Politecnico di Torino

Department of Aerospace Engineering

Master Thesis

Improvement of Electrode Design and Materials for Plasma Antenna Applications

Candidate:
Smoraldi Pasquale

Mentor:
prof. Lorenzo Casalino

TECHNOLOGY
FOR PROPULSION
AND INNOVATION

Under the supervision of:
prof. Daniele Pavarin
dr. Marco Manente

October 2020

Puoi cambiare camicia se ne hai voglia
e se hai fiducia puoi cambiare scarpe.

Se hai scarpe nuove puoi cambiare strada
e cambiando strada puoi cambiare idee
e con le idee puoi cambiare il mondo.

Ma il mondo non cambia spesso,
allora la tua vera rivoluzione sarà cambiare
te stesso.

Contents

Abstract

Improving the performances of a gaseous plasma antenna, in terms of its proprieties, involves complex tradeoffs between plasma parameters. In this context, the efforts conducted in this study were twofold. On one side, a thorough research has been carried out in order to find possible ways to enhance the antenna's performance through the use of electrodes of different sizes. Being the main task to improve the electron density of a GPA with unvaried working conditions, preliminary studies and empirical analysis were performed on readily available commercial electrodes of equal geometry but different diameter, namely T7 and T10. Hereafter, a comparison has been conducted between the previous tests with the ones resulting by a new T10 electrode, characterized by a slightly different shape and the presence of a ceramic collar. Finally, after an attentive literature review, efforts have been made in the direction of suggesting promising materials and coatings to be implemented in future development. The current research will include data analysis obtained from testing some coatings as well. As concerns this aspect, the experimentation has followed two ways: the deposition via sol-gel method and the deposition by sputtering of pills wedged in the extremities of the electrodes.

CHAPTER 1

Plasma Antennas

1.1 Plasma Properties

Plasma can be defined as an electrified gas where the atoms are dissociated into positive ions and negative electrons. However, it is not possible to call "plasma" any ionized gas. A plasma is a *quasineutral gas of charged and neutral particles which exhibits collective behavior* [1].

In a neutral gas, if a macroscopic force is applied it is transmitted to the individual atoms by collisions. The situation is totally different in a plasma because of the presence of charged particles. As these charges move around, local concentrations of positive or negative charge are generated, which give rise to electric fields. Motion of charges creates currents as well, and hence magnetic fields which affect the motion of other charged particles far away. In a plasma, elements exert a force on one another even at large distances; therefore "collective behavior" means that motions depend both by local conditions and on the state of the plasma even in remote regions. [1].

One of the fundamental characteristics of a plasma is its ability to shield out electric potentials that are applied to it. The parameter λ_D defines the *Debye length*, which measures the shielding distance. If local concentrations of charge arise or external potentials are introduced into the system, they are shielded out, leaving the bulk of the plasma free of large electric fields or potentials. [1]

Plasma is a collection of charged particles but, as a whole, it is a neutral body having equal number of electrons and ions. This means that the plasma is neutral enough to define a common unique density, but not so neutral that all the interesting electromagnetic forces vanish. If a fraction of charge from the plasma is removed, it creates a large electric field. In plasma, the *Debye length* defines a length scale over which quasineutrality can be violated and the effects will be shielded if some charge is removed. Given these effects, it is said that plasma is a *quasineutral medium* [2]. A ionized gas can be defined a plasma when it is dense enough that λ_D is much smaller than the system dimensions. [1].

1.2 Plasma Physics

In order to obtain a plasma, the system has to be supplied with electromagnetic energy. Provided geometry, gas properties and the power supply, the plasma density and temperature can be acquired. Talking about plasma density means referring to $10^{18} - 10^{19}$ particles per m^3, about five or six orders of magnitude lower compared to atmospheric pressure. Density is measured in $particles/m^3$ because the values involved are extremely low and, moreover, this parameter does not depend on the type of gas used. As regards temperatures, usually in plasma antenna applications gas, positive ions and electrons have different temperatures. The latter ones, for example, show typical values around 1-2 eV, that is $10 - 20\ 000^o K$, whereas gas and ions have temperatures of about $1\ 000^o K$. This means that the kinetic energy associated with electrons is much bigger than the one related to neutral and positive particles. Such behaviour can be explained by the fact that collisions between atoms are reduced because of the low number of particles, thus leading to a non-uniform distribution of energy among the species.

Given a distribution of neutrals, it is essential to evaluate the probability that an electron, launched towards a certain direction, hits a neutral. This probability depends on the number of electrons and neutral, on the type of collision, on the distance between particles and on their dimensions. For this reason the concept of *cross section* is introduced, that is an equivalent area that surrounds the neutral. If the incoming electron passes within this surface, then a collision occurs; otherwise, there is no collision. Another important concept is the *mean free path*, that is the average distance covered by a particle before a collision and it depends on two factors: the neutral density and the cross section. The greater is the number of particles and the smaller is the cross section, the shorter is the distance to be covered to let the collision occur. It is also essential to take into account the *collision frequency*, that expresses the average frequency at which a collision happens and it is inversely proportional to the mean free path and directly proportional to the particle's speed.

The concepts introduced are useful to define a new fundamental parameter for plasma antennas, namely the *reaction rate*, which indicates the number of ionizations that occur within the discharge. This quantity depends on the number of electrons and neutrals and on the product between the cross section and the velocity. Indeed, the gas has a greater tendency to ionize the bigger are the number of particles, their kinetic energy and cross section. Essentially, there exist two basic phenomena which regulate the formation of plasma: chemical reactions and wall losses.

1.2.1 Chemical Reactions

The most important chemical reaction for plasma antenna applications is definitely ionization, which takes place when an electron collides with a neutral and divides it into a positive ion and another electron.

The excitation of a neutral does not have a positive effect on the plasma performances as it depletes the energy provided to the system in order to ionize the neutral, but after a few moments the excited electron return in its equilibrium state emitting the absorbed energy by means of luminous radiation. As a matter of fact, the color of the plasma during the discharge is the index of the excitations occurring inside the plasma discharge itself. As the purpose is to realize a plasma that is as much ionized as possible, its color expresses a sort of loss of the provided energy. If the plasma were totally ionized it would show no color at all. Therefore, it is a mistake to associate the radiation intensity with the plasma density. This type of connection could exist for low levels of ionization only because with a greater number of free electrons there is a higher probability that an excitation or a ionization takes place.

In general, it is expected that about 20% of the total energy is employed in ionization. Another significant percentage, 10-15%, is used for excitation and the luminous radiation corresponds at about 10% of the total energy. Much more energy is depleted by wall losses. To sum up, at least the half of the provided energy is wasted in heat leaks. The energy required for the ionization of an argon atom is about 12 eV, while, on average, the electron temperature is around 1 eV. However, ionization occurs anyway and the reason can be found introducing the *Boltzmann distribution*. It is a bell-shaped curve which indicates that there is a high probability to have particles with a velocity similar to thermal agitation, but there exists even a chance to have very high-velocity particles. This explains why there is a small quantity of electrons which allows the ionization even if the average particles' temperature is around 1 eV.

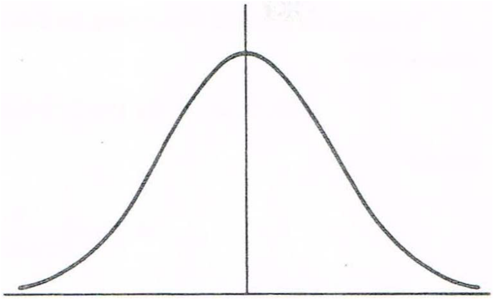

Figure 1.1: Boltzmann Distribution

1.2.2 Plasma-Wall Interaction

In a conventional gas, if a particle hits a wall, it bounces back. On the contrary, in a plasma there is a high probability that the incident particle takes an electron from the wall or, on the other hand, that an electron is absorbed by the wall itself and this is called "wall recombination". As the particle/electron is lost when it recombines, it can be understood how delicate the plasma-wall interaction results. Once the power is removed the plasma turns off as the charged particles therein undergo wall recombination. It is hence necessary to generate a sufficient number of ionizations in order to prevent the plasma from switching off. This is done by providing electromagnetic energy for accelerating the particles so that a neutral is ionized when hit by an electron. Particle acceleration due to the applied voltage leads to collisions which reduce the quantity of energy. Even wall collisions can be considered as losses because from a charged particle a neutral is obtained, thus losing the quantity of energy provided to ionize it.

When referring to the interaction between particles composing the plasma and the wall which confines them, essentially it is the concept of *sheath* that is being discussed. One of the plasma properties is to be quasineutral, that is globally neutral as the number of ions and electrons are equal. However, this is not true near the wall. The main reason is that electrons are much more movable than positive ions because their average temperature, and thus their velocity, is much higher. Near the wall recombination occurs and this means losing half of the Boltzmann distribution represented in Figure 1.1. As the electrons are faster than ions, initially many electrons are lost due to the interaction with the wall, thus resulting in a globally neutral plasma with an excess of positive charge at the walls. Consequently, the potential fall generates an electrostatic field which accelerates the ions towards the wall while electrons are decelerated. In conclusion, the system tends to equilibrate itself by creating an electric field which slows down the flux of electrons lost because of the plasma-wall interaction and compensates for it with an acceleration of positive charges that are lost at the wall. A consequence of this concept is the decrease of the plasma density near the wall and the losses associated with it are significant. This means that tens of percentage points of the total energy turn into thermal dissipation which heats the wall. In the case of the present application, such wall consists in a vial within which the plasma is stored.

1.3 Plasma Dynamics

There exist several ways that can lead to the ionization of particles even in standard atmosphere at room temperature, such as cosmic rays or high-energy particles which ionize by collision. The Saha equation points out the amount of ionization to be expected in a gas in thermal equilibrium [1]:

$$\frac{n_i}{n_n} \approx 2.4 \cdot 10^{21} \, \frac{T^{\frac{3}{2}}}{n_i} \, e^{-\frac{U_i}{KT}} \tag{1.1}$$

Here n_i and n_n are, respectively, the density (number per m^3) of ionized atoms and of neutral atoms, T is the gas temperature in ^oK, K is Boltzmann's constant, and U_i is the ionization energy of the gas, that is, the number of ergs required to remove the outermost electron from an atom. For ordinary air at room temperature the fractional ionization n_i/n_n predicted by Eq. (1.1) is ridiculously low [1]:

$$\frac{n_i}{n_n} \approx 10^{-122}$$

Using two electrodes and an appropriate potential difference, one would measure for ordinary air an extreme low current ($\approx 10^{-10}A$).

1.3.1 Plasma Discharge

The plasma discharge takes place at the time when, using two electrodes, a potential difference is created. This voltage accelerates the particles from an electrode to another. In the plasma antenna applications the system operates at frequencies of tens of kHz and for such values the magnetic fields which generate are negligible if compared with the electrostatic effects.

One of the most important issues in the application of plasma antennas is the ability to evaluate the reaction of the plasma to an external signal. The introduction of a wave sets in motion especially electrons which collide with ions if the collision frequency is high enough. The more collisions occur, the less electrons move and the more damped the wave results. On the other hand, if the plasma density is low, few particles vibrate and the amplification of the signal is not efficient. Therefore, the collision frequency has to be high enough to generate the plasma discharge, but not too much to prevent the wave being too damped, thus permitting the signal propagation.

1.3.2 Discharge Types

There are several types of discharge that generate when a current between two electrodes is introduced. There are three main distinctions:

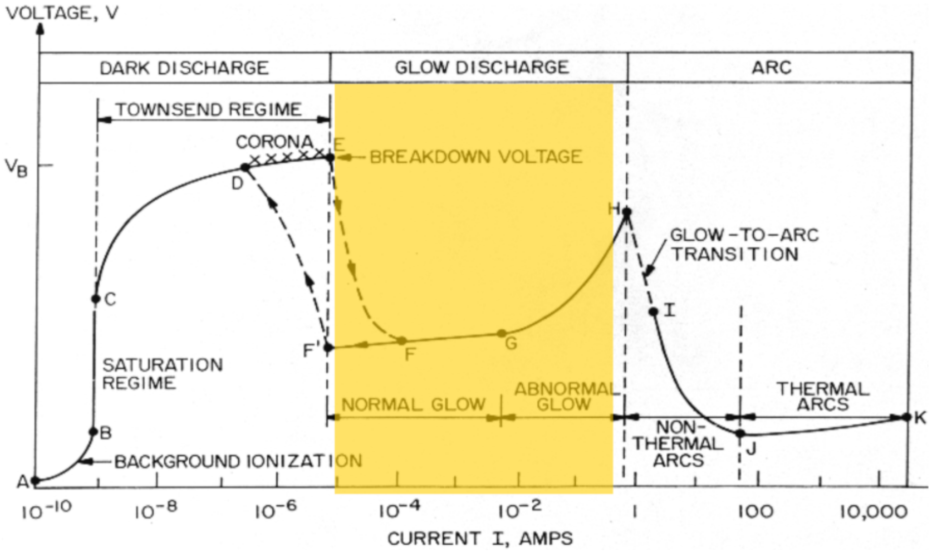

Figure 1.2: Discharge Types

- Dark Discharge. In this region the discharge is substantially turned off. The gas is ionized by a radiation source. As the voltage is slowly increased, random bursts are caused: randomly produced ions in the gas are accelerated towards the strong negative field of the cathode, where they cause the emission of secondary electrons [3]. when the breakdown criterion is satisfied, ions arrive in sufficient quantities and gain enough energy that additional carriers are freed during the subsequent ionization caused by the acceleration of the secondary electrons from the cathode, by their collision with neutrals [3]. This process is called Townsend avalanche.

- GLOW DISCHARGE. This is the region of visible light, in which the carrier generation process reaches a point where the average electron leaving the cathode frees another electron. The voltage drop to the normal glow discharge maintaining voltage is caused by a build up of space charge. The external field becomes distorted by the presence of the charge, which leads to the generation of the normal glow discharge region, where an increase in current of several orders can be realized for no change in voltage. Once the area reaches its maximum, an increase in voltage would be required for an increase in current. [3].

- ELECTRIC ARC. It is a prolonged electrical discharge characterized by a very high current density and the emission of visible light. Electrons leave the cathode by thermionic emission and field emission, and the gas is ionized by thermal means [4]. An arc is distinguished from a glow discharge because of a lower voltage. Moreover, the effective temperatures of both electrons and positive ions are approximately equal in an electric arc, whereas ions have much less thermal energy than the electrons in a glow discharge.

The *breakdown voltage* is the value at which the discharge turns on, that is the transition to the dark space discharge region to the glow discharge. If an over voltage $V > V_{breakdown}$ is applied, the voltage drops within a fraction of a second to the sustaining voltage. This explains the fact that the inverter which converts the DC power supply into the high frequency AC current required by the CCFL must supply a very high voltage to start the lamp, which rapidly drops to the normal voltage [3].

1.4 Secondary Emission

When a ion hits the wall, it can happen that the latter, in addition to the neutralization of the ion, releases an electron. Therefore, an effect of secondary emission can be generated by bombarding the wall with ions. The higher is the incident ion energy the greater is the emission of secondary electrons. It is much easier to use this phenomena on the electrodes than the wall, where the potential difference is about only $10 - 20\,V$. The electrodes, instead, are designed to oscillate at voltages around the hundreds of Volts, thus the plasma is more accelerated and the effects are more intense compared with the walls. However, researches have proven that, by the use of suitable materials, it is possible to aim at appreciable levels of secondary emissions even on the walls.

1.5 Townsend Criterion: Avalanche

Accelerating the electrons in the gas with a voltage generated by means of two electrodes, they collide with neutral particles and ionize them. Consequently, the number of electrons within the gas raises. If the potential difference is sufficient, both the incident electron and the other one freed by ionization collide in turn with other two neutral atoms. This leads to their ionization and other two new electrons are obtained.

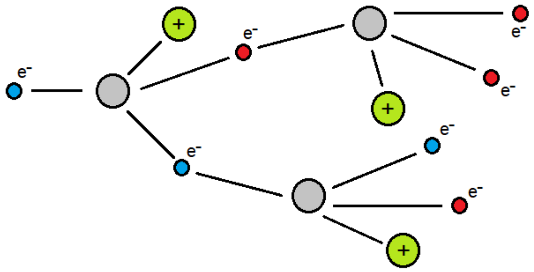

Figure 1.3: Electron Avalanche

Therefore, if the density of the electric field is high enough, there is an exponential increase of free electrons along the discharge given by the electric field action. In order to quantify this effect, the *Townsend's first ionization coefficient* α is used, that is the number of ionizing collisions of electrons per unit length.

The variation of the particle flux is proportional to the number of particles multiplied by the reaction coefficient. The greater is the mean free path the lower is the probability to collide. Townsend's first ionization coefficient even depends on the particle's inclination to ionize and it is therefore related to the energy necessary for the ionization of a gas. Lastly, a dependence on the local electric field can be noticed, i.e. the potential difference between the electrodes. In conclusion, the dynamic of ionization is mainly caused by two factors: the electric field E and the pressure of neutrals p.

The voltage applied produces the emission of a flux of electrons from the cathode. However, even some ions collide with the electrodes, which creates an additional contribute of particles due to the secondary emission phenomenon. Thereafter, because of the avalanche criterion, the flux sees its intensity exponentially raised until it reaches the anode. It can be therefore understood how important the choice of an appropriate material is for the cathode as it defines the secondary emission. Whereas, the gas mixture affects the avalanche phenomenon. As the flux of electrons advances, on the one hand the ionizations generate positive ions attracted towards the cathode (which further raises the secondary emission), while on the other hand it creates free electrons that intensify the flux towards the anode, where an increased concentration of negative charges will hence be present.

The concepts just exposed are summarised and verified by the relation of the current that is gradually collected at the anode, which results to be the same of that emitted by the cathode:

$$\Gamma_{ea} = \frac{e^{\alpha d}\,\Gamma_{eo} + (1+\gamma)\,\dfrac{S_e}{\alpha}\,\left(e^{\alpha d}-1\right)}{1-\gamma\,\left(e^{\alpha d}-1\right)} \tag{1.2}$$

where d is the distance between the electrodes and γ is secondary electron emission coefficient due to ion impact (Penning effect). It can be noticed how the total current depends on the one initially emitted plus the current due to secondary emission multiplied by an exponential which is function of $\alpha\, d$.

1.5.1 Voltage Breakdown

The avalanche dynamic is correct until a real plasma discharge sets in. When this happens, the theory previously introduced is not totally correct. Indeed, in order to create a plasma discharge, currents in the order of magnitude around $10^{-1} - 10^{-2} A$ are considered, certainly much higher than the ones taken into account so far (currents of about $10^{-10} A$ can be measured from the ionization of particles in standard atmosphere). This means that the denominator of Eq. (1.2) tends towards zero. Therefore, Townsend's criterion states that the breakdown condition is given by [3]:

$$\gamma\, e^{\alpha d} = 1 \tag{1.3}$$

Being γ given by the material, at a fixed distance between the electrodes, to power up the discharge the coefficient α, which depends on the electrostatic field pressure, has to be modified until the relation (1.3) is satisfied. Thus the expression for the voltage breakdown can be obtained [3]:

$$V_b \simeq \frac{pd}{\ln\left(\dfrac{pd}{\ln\left(1+\gamma^{-1}\right)}\right)} = f(pd) \tag{1.4}$$

where $V_b = E \cdot d$ is the voltage breakdown. Equation 1.4 is called *Paschen Law.*

1.5.2 Paschen Curve

Physically, the breakdown voltage is a function of the product between pressure and distance among the electrodes and it follows the trend shown in Figure 1.4. The illustrated curves are named after *Paschen curves*.

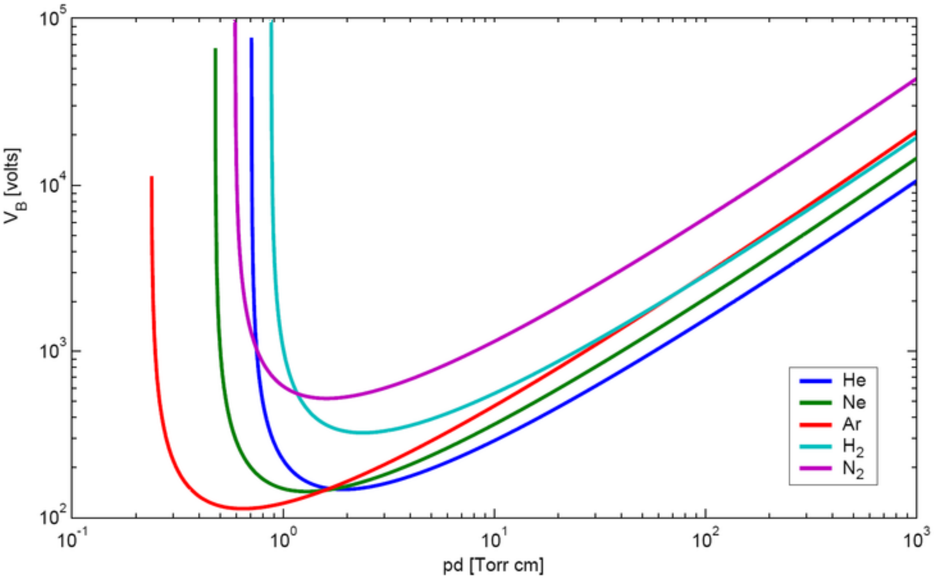

Figure 1.4: Paschen curves for different gasses

It can be noticed that the curves show a minimum. For too high or too low values of the product *pd* the quantity of voltage needed to turn the discharge on rises greatly. This happens because if the pressure is excessively high the number of particles grows so much that the mean free path is too small to let the particles ionize the gas. On the other hand, if the pressure is excessively low the number of particles is not sufficient to ionize the gas because, even if electrons are much more accelerated, the collisions against neutrals essential for ionization are very rare. When reducing the pressure, the Paschen curve tends to move downward and the discharge starts at lower voltages. A similar argument can be made concerning the distance between the electrodes. As regards the part of the curve on the right of the mininum, reducing the distance *d* maintaining the same voltage means a greater electric field *E*. Therefore particles are more accelerated. Conversely, if *d* rises too much the resulting electric field is smaller and the acceleration received by each particle is lower. The evolution of the curve on the left of the minimum can be explained simply by observing that, decreasing d, at a certain point the distance between the electrodes becomes much smaller than the mean free path and there is no time to let collisions happen.

In conclusion, the breakdown voltage is a good parameter in order to evaluate an improvement or deterioration of the plasma density because activating the discharge earlier means generating a greater flux of electrons or having a gas more inclined to ionize. By observing Figure 1.2 it can be noticed that, once the discharge has started, the voltage necessary to sustain a certain level of current is lower than the breakdown voltage since the plasma is much more conductive than the gas because of the presence of free charges.

1.6 Antenna Fundamentals

The purpose of an antenna is to convert, through electrodynamic induction, an electromagnetic wave travelling in free space into an signal [5]. It can be easily understood how crucial the evaluation of antenna parameters is in order to make the device work under optimal conditions. Care must be taken to power coupling, which means paying attention to drive frequency tuning and input voltage. For radiating elements, impedance is one of the most critical aspects. This parameter defines the overall efficiency in terms of power transfer. Figure 1.5 shows, from an electrical point of view, the simplest antenna system (generator, lossless transmission line, antenna).

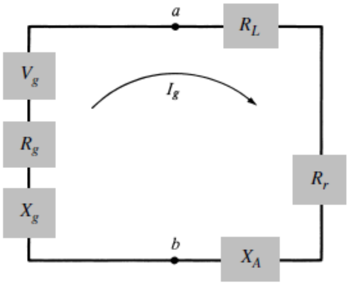

Figure 1.5: Thevenin equivalent for the antenna circuit

V_g is the source (signal generator/transmitter) with internal impedance $Z_g = R_g + jX_g$, while the antenna is a passive component (in transmission mode, otherwise the symbols are inverted) with $Z_A = (R_L + R_r) + jX_A$. It is possible to obtain the maximum available power at the generator delivered to the antenna if two conditions are satisfied [6]:

$$R_r + R_L = R_g \qquad \text{and} \qquad X_A = -X_g$$

About half of the total power is dissipated on Z_g, thus the available power at the source cannot be more than the remaining half. This power has still to be radiated in free space. It was imposed that all the available power from the source would be at the input terminals of the antenna. Anyway, internal losses within the antenna (R_L) are supposed to absorb an additional amount of energy. The fraction of EM radiated power can be written as:

$$Pr = Pg\,\frac{R_r}{R_L + R_r}$$

where R_r is the radiation resistance, defined as a fictitious quantity which can be thought as a resistance that, instead of dissipating power through Joule heating, emits EM waves. In order to perform in ideal conditions, it should be $P_r \to P_g$ and therefore $R_L \to 0$. It should be noticed that this analysis was performed in transmitting mode; as concerning the receiving mode, the antenna becomes the source.

Another among the most important parameters necessary to define the overall capabilities and performances of an antenna is the radiation pattern, which is representative of the relative field strengths of the field radiated by the antenna [7] and it always plotted in the far field region.

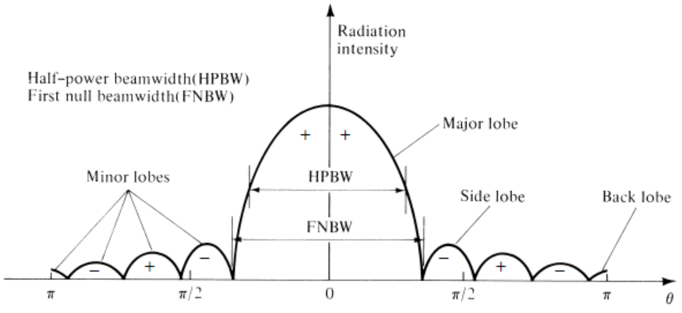

Figure 1.6: Radiation Pattern [8]

The graphic shown in Figure 1.6 is a function of the directional coordinates and correlates the value of a physical quantity, calculated on a surface of constant radius with respect to the observer's position, with the angular coordinates θ and ϕ [8]. The plot displays the following quantities: polarization, power flux, field strength, radiation intensity and directivity. Antennas can be therefore classified depending on the plot shape:

- Directional (i.e. reflector antenna, an example may be Figure 1.6);
- Omnidirectional (i.e. dipole, large mesh in Figure 1.7 and solid gray in Figure 1.8);
- Isotropic (i.e. ideal punctual antenna, fine mesh in Figure 1.7 and striped pattern in Figure 1.8).

Usually, for reflector antennas the polar radiation pattern is used, in order to better characterize the position of their main lobe and, possibly, steerability. Instead, as regards dipoles and isotropic antennas, they have the same 2D plot on the $z = 0$ plane and thus using 3D graphs may be more helpful.

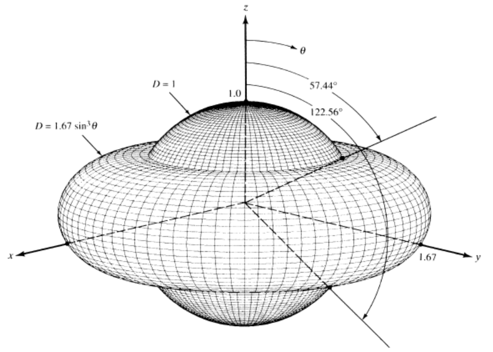

Figure 1.7: 3D Radiation Pattern [8]

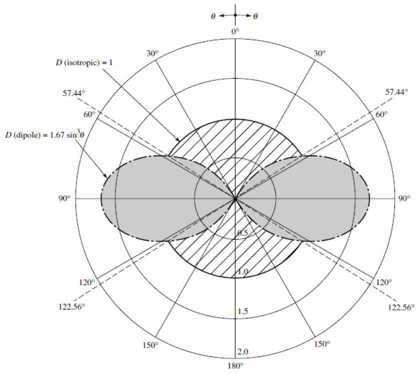

Figure 1.8: Polar Radiation Pattern [8]

Another crucial parameter can be deduced from these graphics: the directive gain, or *directivity* D, which can be defined as the ratio of the radiation intensity in a given direction from the antenna to the radiation intensity averaged over all directions. The average radiation intensity is equal to the total power radiated by the antenna divided by 4π. The directivity of a non-isotropic source is equal to the ratio of its radiation intensity in a given direction over that of an isotropic source [8].

$$D = \frac{U}{U_0}$$

where U is the radiation intensity in a given direction and U_0 is that of an isotropic source.

Of equal importance is the *gain*, being defined as the ratio of the intensity, in a given direction, to the radiation intensity that would be obtained if the power accepted by the antenna were radiated isotropically. The radiation intensity corresponding to the isotropically radiated power is equal to the power accepted (input) by the antenna divided by 4π [8].

$$Gain = 4\pi \frac{\text{radiation intensity}}{\text{total input (accepted) power}}$$

Usually the gain is expressed in terms of dBi, that is decibels over the gain of an isotropic source.

The last aspect that should be taken into account is the structure of the field radiated by an antenna on the basis of the distance from the radiator. The most important distinction to be made is between radiative/near field and far-field. In the first one the EM wave and the radiator still exchange reactive power due to the mutual coupling of radiation and currents on the surface of the antenna. Consequently, each relevant parameter to the antenna analysis is calculated at far field conditions ($r > 10\lambda$), where λ is the wavelength and r is the distance from the radiator.

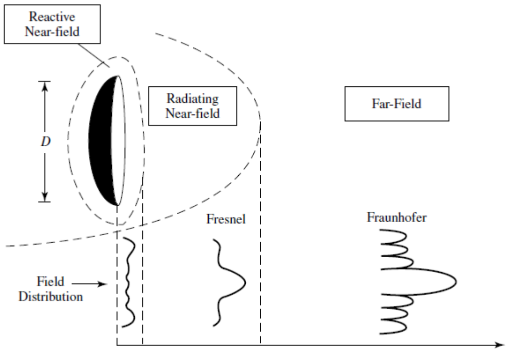

Figure 1.9: Radiating regions [8]

1.7 Gaseous Plasma Antennas

Traditional antennas exploit metallic components to transmit and/or receive electromagnetic waves. A gaseous plasma antenna (GPA) can be defined as a device that relies on a weakly or fully ionized plasma (rather than on metallic conductors) to either radiate or receive electromagnetic (EM) waves [9]. The plasma discharge used as radiating element is usually confined into a dielectric vessel such as a glass cylinder or other enclosures that may come in different shapes [9]. Plasma can be artificially generated from gas by various excitation means, like by heating the gas or exposing it to a strong electromagnetic field until it becomes ionised and increasingly electrically conductive. The plasma, when it is turned on, behaves like an electric conductor since the electrons orbiting atomic nuclei are stripped away, thus creating free electrons (whose number is related to the gas temperature and density). This allows the plasma to transmit and receive EM signals.

Plasma antennas show several potential advantages over conventional metal antennas as their properties can be controlled electrically rather than mechanically. This makes plasma antennas appealing for a wide range of applications. First of all, when the plasma is turned off, it reverts to to a neutral gas confined in a dielectric enclosure and so it stops behaving as a conductor. This implies that GPAs have a low radar cross section, thus being transparent to any electromagnetic wave whose frequency is above the plasma frequency. This feature makes plasma antennas interesting when dealing with applications that need many antennas or antenna arrays that operate at different frequencies. In this contest GPAs represent a compelling alternative to their conventional counterparts since they can provide significantly lower mutual coupling values among the different arrays. As a matter of fact, unenergized plasma elements do not interfere with active ones, and therefore the coupling among plasma antennas working at different frequencies becomes very low. Moreover, plasma elements can be energized and turned off on time scales of microseconds [9]. In addition, GPAs are rapidly reconfigurable electrically rather than mechanically with respect to the operation frequency, gain, radiation pattern and input impedance. This means that their radiation properties can be changed by electrically controlling the plasma parameters (e.g., density) [9].

Even though plasma antennas have some interesting advantages with respect to their metallic counterparts, manufacturing and costs are much more demanding. Performances are based on hard-established trade-off between different parameters. Although, ultimately, it is desirable to have a plasma density as high as possible while keeping other factors (e.g. Joule heating of the glass enclosure, power consumption and collision frequency) unvaried. This reflects on the complex ionization processes that take place within the plasma itself [10].

Furthermore, the usage of plasma discharges as antennas in communication systems can be hindered by several issues. The noise introduced by the plasma generation technique is a major issue that has considerably hampered the use of this technology. However, the introduction of RF surface wave and pulsing power technique made it possible to obtain lower noise levels, higher plasma density and reduced power consumption [11].

Another obstacle to the adoption of GPAs is constituted by their complexity. These antennas, indeed, even include the components used to generate the plasma as metallic electrodes and wires. This equipment has an impact on the antenna performances, specially on its operation frequency.

Other critical aspects concerning the realization of an actual plasma antenna are the availability of suitable technological solutions to ignite and sustain the plasma, and the capability of developing customized dielectric vessels whose shape and dimensions must be carefully chosen according to the antenna type and operating frequency.

The design of a plasma discharge includes a cylindrical glass vessel with a length that varies from 34 mm to 100 mm, a diameter of 4 mm, and a thickness of 1 mm, and short cylindrical electrodes of a thickness of 1mm.

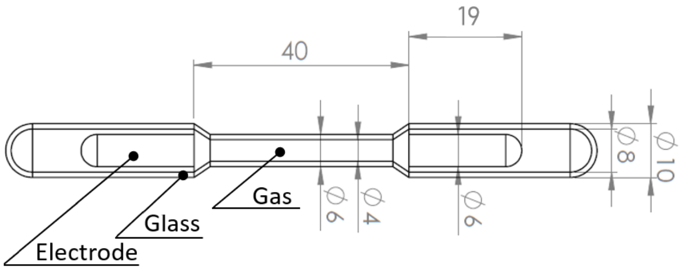

Figure 1.10: CAD model of a generic plasma discharge [12]

1.7.1 CCFLs

Cold cathode fluorescent lamps (CCFLs) consist of a glass cylindrical tube filled with a Penning gas mixture of noble gases or nitrogen and a small amount of mercury. Two electrodes, usually made from nickel or a refractory metal, are placed at both ends of the tube in order to establish electrical connection. When a high voltage at high frequency is applied to the electrodes, the gas dissociates and several processes occur, leading to the formation of a plasma. The strong emission of UV light caused by the excitation of the mercury is converted into visible light by the phosphor, which is coated onto the inside of the tube [3].

CCFLs work following Paschen's law (Section 1.5), specifically in the normal glow region (point G in Figure 1.2). Once the breakdown criterion has been satisfied, which means that enough power is coupled to the tube through metal wires soldered to the electrodes, ions arrive in sufficient number and with enough energy that more are created by the subsequent ionisation caused by the acceleration of the secondary electrons from the cathode, by their collision with neutrals [3]. Therefore, a column of ionized gas creates a path for the current to flow, making the vessel similar to a simple wire capable of radiating AC signals.

Most of the preliminary work was performed using components designed for CCFL lamps due to the readily availability of such devices on the market. Every adjustment applied afterwards can be considered as an improvement upon this original concept.

1.7.2 Hollow Cathode

The concept of hollow cathode has been successfully implemented for ion and Hall effect thruster applications. Nevertheless, its working principle has been proven to be suitable for gaseous plasma antennas as well.

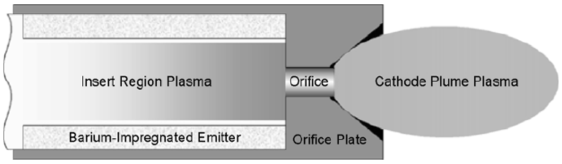

Figure 1.11: Schematic configuration of a hollow cathode discharge [13]

Figure 1.11 shows a typical hollow cathode structure. The main advantage of this configuration is that the electron space charges are neutralized by plasma ions generated throughout the device, thus allowing for higher current outputs at a given operating voltage, compared with vacuum cathode thrusters. Such feature is carried out thanks to the highly thermoemissive material in the insert region, which sustains such high intensity electron flux. As a matter of fact, the intense ion bombardment of the cathode leads to very hot cathode surfaces and consequent thermionic emission. Moreover, the set-up, as presented in Figure 1.11, allows the achievement of higher plasma and neutral pressures with low electron temperatures. Therefore, as the ion energy at the insert is reduced, the plasma potential inside the hollow cathode is low.

Hollow cathodes are usually enveloped in the keeper, that is another electrode the purpose of which is to facilitate the discharge ignition and to preserve the cathode temperature and operation in the event of unexpected interruptions. The keeper has proven to be helpful in preventing degradation from stray high-energy ion bombardment. Lastly, it should be remarked that hollow cathodes work in self-heating mode since the plasma bombarding itself warms up the cathode insert rather than the heater, which is turned off during operation. The dominating heating process depends on the discharge current, cathode geometry and the internal gas pressure in the insert and orifice region.

1.7.3 Prototypes under development

A full depiction of the prototypes and purposes on which the present research focused will be portrayed in this Section. The current endeavour involves plasma discharges based on CCFL technology, that means having the same working principle and field distribution as a common lamp, even if the purpose is different. Indeed, the starting configuration of GPAs provides for the employment of readily available CCFL electrodes immersed in a known gas and enclosed in custom designed glass vessels of various lengths.

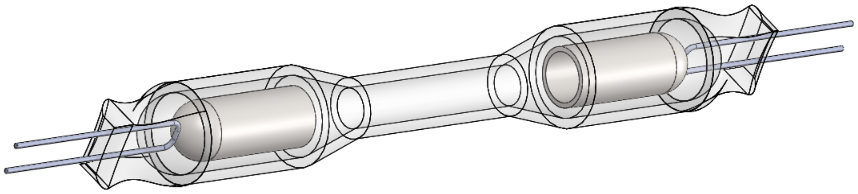

Figure 1.12: CAD model of a generic vessel [12]

The primary components of any vessel are the two electrodes and the glass enclosure. Several variations of CCFLs have been developed depending on the size of either of them. For example, the length of the latter, calculated as the distance between the electrodes, ranged from a minimum of 34 mm to a maximum of 100 mm: shorter vessels were used for the dipole design while longer ones made up the reflector array set-up. Computer simulations have proven, in accordance with Paschen's law (see Section 1.5), that values of length shorter than 34 mm would impede ignition at the working pressure of 1.5 mbar. The glass enclosure is bulged at both ends to host the shells, while the portion of the vessel that accommodates electrodes is fixed since its design already optimizes the use of space, even if the overall length of the casing might be variable. The latter consists of a cylindrical hollow structure 1 mm thick made of soda-lime glass. The enclosure by itself weights less than 10 grams. The vessels studied and tested in the present work mostly collocate in the range of 40-50 mm. The shell is a CCFL-compliant electrode, featuring an hollow cylindrical structure with a semi-spherical cap 0.5 mm thick, with a wire bent and soldered to the metal. A close-up of the electrode has been included in Figure 1.13 to better show its hollow structure and shape.

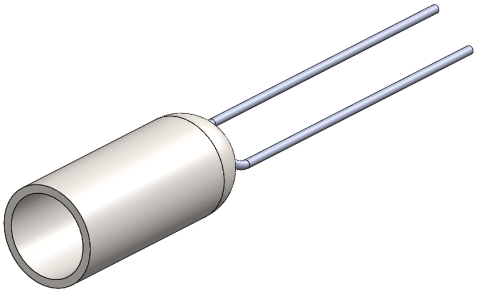

Figure 1.13: CAD model of a generic shell

Early designs involved the use of readily available CCFL lamps. Hereafter, the great potential shown by the application and the success achieved encouraged to move towards custom-designed vessels, which allows to handle several features like length, shape, gas mixture, enclosure coating and electrode design and covering. As a matter of fact, the purpose of CCFL lamp technology is to optimize luminosity, while the goal of the current study is to enhance the electron density in the plasma discharge.

For completeness, it should be remarked that the object in Figure 1.12 has to be considered as a module used in conjunction with other components to form a radiating element. Below, two hypothesis of what a cross-dipole setup and a transmit array design are thought to be.

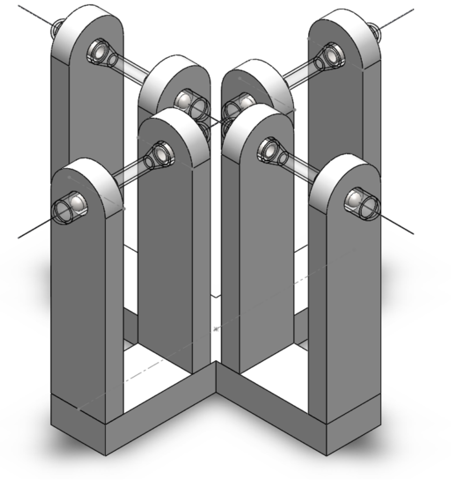

Figure 1.14: CAD model for a cross-dipole setup

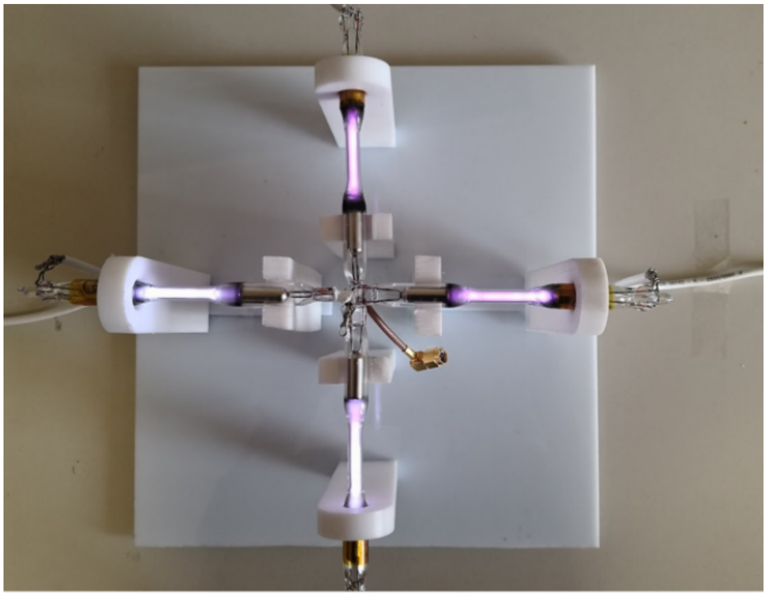

Figure 1.15: Picture of a cross-dipole in ON mode

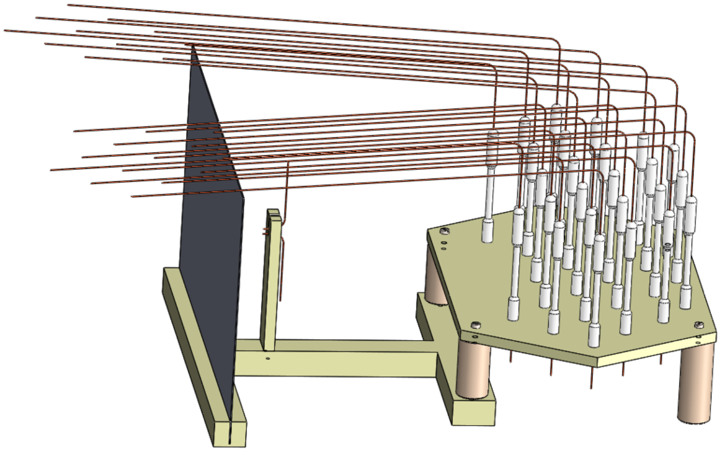

Figure 1.16: CAD model for a transmit array design

CHAPTER 2

Literature Review

2.1 Problem Statement

Improving the performances of a gaseous plasma antenna, in terms of its proprieties, involves complex tradeoffs between plasma parameters. In this chapter, a thorough research has been carried out in order to find possible ways to enhance the antenna's performances by covering the electrodes through innovative materials. Therefore, being the main task to improve the electron density of a GPA, the aim pursued in the following Chapter was to suggest promising materials and coatings to be implemented in future developments, after an attentive literature review. The current section will face, initially, the problem of sputtering and, at a later time, the theory behind secondary emission. Moreover, some observations about coating thickness and roughness will be included as well. Finally, a few alternative deposition methods will be identified, among which one will be chosen as a comparation technique with the Sol-Gel method, discussed later in Chapter 4.

2.2 The Phenomenon of Sputtering

Ionized gases are accelerated towards the electrode, where they release electrons by the process of secondary electron emission. Kinetic energy is transferred to the electrode surface atoms, resulting in electrode heating and erosion (sputtering), and electrostatic interaction between the electrode surface atom and the ion results in electron emission [14]. The released electrons are accelerated away from the electrode and gain sufficient kinetic energy to cause further ionization events. At a certain voltage, eventually, a sufficient number of ions is generated, the ionization can be sustained and breakdown occurs [15]. It is easy to predict the beginning of sputtering after a while as the main purpose of the cathode is to be bombarded by energetic ions. However, this phenomenon can compromise the operation of the device.

Sputtering is a transfer of kinetic energy from the impinging ion to the surface of the material, for which an energy transfer function is given for a binary collision by classical mechanics (2.1), where m_p is the mass of the projectile, m_t is the target mass and E is the ion energy [14]:

$$T(E) = \frac{4\,m_p\,m_t}{\left(m_p + m_t\right)^2}\,E \tag{2.1}$$

Unfortunately, the sputtering phenomenon involves a complex cascade of collisions at the surface and it is not a binary process. Moreover, the sputter yield depends on the nuclear stopping distance, that is an indicator of the quantity of energy deposited into the surface layers.

Sigmund [16] proposed a model which reasonalby estimates the sputter yield as inversely proportional to the energy of sublimation for the material U_0:

$$T(E) = \frac{3\alpha}{4\pi^2}\,\frac{4\,m_p\,m_t}{\left(m_p + m_t\right)^2}\,\frac{E}{U_0} \tag{2.2}$$

The function α is defined as:

$$\alpha \simeq 0.124\,\frac{m_t}{m_p} + 0.158 \tag{2.3}$$

Therefore, Eq. (2.2) would suggest the use of high atomic mass materials and with a high energy of sublimation. For these reasons refractory metals have long been a popular choice for cold cathode material.

Sputtering is quantitatively described by the sputter yield as the average number of ejected particles per incident particle [17]. The sputter yield is very important for lifetime estimations. The sputter yields of ceramic materials, i.e. quartz, alumina (Al_2O_3) and Boron Nitride (BN) under normal xenon ion incidence at 100, 250, 350, 500 and 800 eV are presented in the experiments in [17]. The results are given in mm^3/C, corresponding to the removed volume per Coulomb of incoming particles. Figures 2.1, 2.2 and 2.3 show the sputter yields of quartz, alumina and boron nitride under normal xenon ion incidence in comparison with other published data [18] [19] [20] [21] [22] [23] [24].

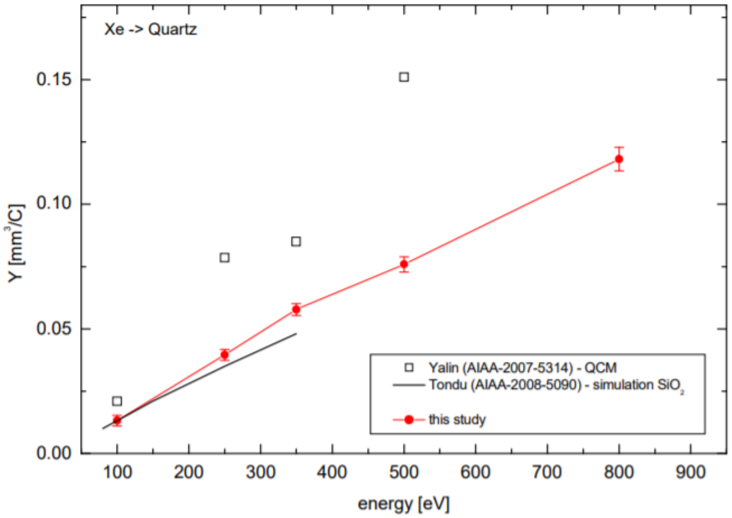

Figure 2.1: Sputter yield of quartz in dependence on xenon ion energy.

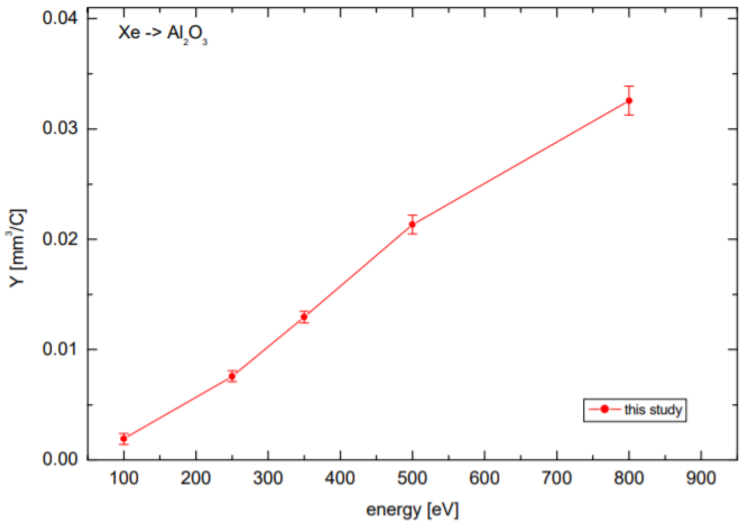

Figure 2.2: Sputter yield of alumina (Al_2O_3) in dependence on xenon ion energy.

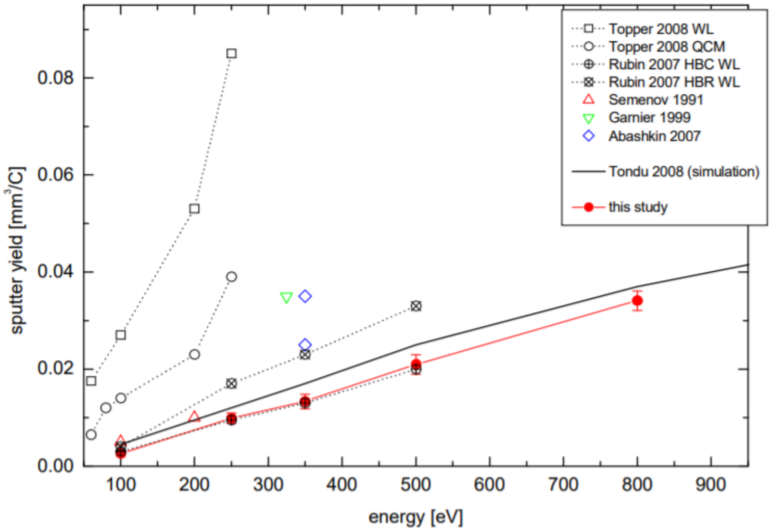

Figure 2.3: Sputter yield of BN in dependence on xenon ion energy.

2.3 Secondary Emission Yield

The process of secondary emission involves several factors. As a matter of fact, due to the complexity of the phenomenon, several theoretical and numerical models have been developed in order to predict the features of secondary electron emission.

To mention a few, the secondary electron yield as a function of primary electron energy [25] and the energy distribution of the secondary electrons [26]. The main flux into which such phenomenon can be summarized consists in: primary electron penetration, carriage of the internal secondary electron to the surface and the secondary electron escape process from the material surface. As regards the first step, primary electrons are assumed to move in a straight-ahead path. During their motion, they are slowed down by collisions with ions and electrons. Throughout this process, kinetic energy is transferred thus leading to generation of secondary electrons.

Theories reported in [26] and [27] define $N(x)$ as the energy loss in the layer dE divided by the average excitation energy B, that is the number of secondary electrons produced in the layer dx. The final equation can be written as:

$$N(x) = \left(\frac{A}{2}\right)^{\frac{1}{n+1}} \frac{1}{B(R-x)^{\frac{n}{n+1}}} \tag{2.4}$$

where A is a constant and R is the maximum penetration depth, which can be expressed as follows:

$$R = \frac{E_0^{n+1}}{A(n+1)}$$

where Eo is the primary electrons initial energy.

By the analysis of expression (2.4) it can be deduced that it is important to raise the secondary electron production in correspondence with the end of the primary-electron path. Additionally, by the definition of R it is clear that primary electron penetration depth increases with the initial energy.

Even the phenomenon of elastic backscattering has to be taken into consideration as concerns the penetration of primary electrons, according to which secondary electrons reverse their motion, escaping through their original trajectories. Hence, the yield from elastic backscattering is the ratio of the flux of inelastically backscattered secondaries to the flux of primaries [28]. Secondary electrons are transported throughout the material either by a single-scattering process or by a diffusion process where a large number of scattering events is involved. Generally, a high-energy primary electron can generate several secondary electrons, which lose energy through the excitation of valence electrons into the conduction band [29]. The inner working of internal secondary electron loss of energy depends on the material.

Finally, the last aspect which characterizes the phenomenon is the secondary electron escape process at the solid-vacuum interface [29]. The Secondary Electron Emission Yield (SEEY) can be defined as the ratio between the primary electron flux which hits the surface and the secondary electrons escaping from the solid-vacuum surface. Nevertheless, the results found in literature show several variations in the set-up developed, in the measurement technique and in definition of SEEY itself [30]. This explains why, for a given material, its value may change on the basis of the the sample preparation and handling, the implemented set-up, the angle with which the ion beam impacts the specimen, the measurement procedure and the numerical model and assumptions made as well.

For example, in the work shown in [31] and [32], a cleavage tube with an internal coating of tin oxide as an electron collector has been used. The primary pulse was measured with the help of a suppressor grid negatively biased relative to the target, while the secondary current was measured with the grid positively biased with respect to the target. The SEEY is taken as the ratio of the secondary pulse to primary pulse measured. A similar setup was adopted in [33] for the measurement of secondary electron emission from organic compounds.

In their work, *Tartz et al.* [17] proved that the secondary electron emission coefficient (SEEC) for electron impact is larger for molybdenum than for aluminum. The coefficients apparently differ at energies above 50 eV.

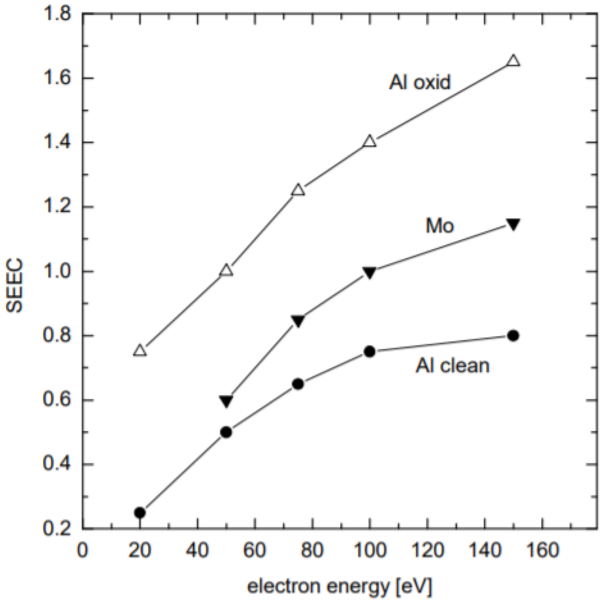

Figure 2.4: Secondary electron emission coefficients in dependence on electron energy.

Generally, the secondary electron yields observed do not present high values due to the fact that internal secondary electrons lose most of their energy colliding with electrons and ion. In addition, the transport of secondary electrons is crucial in order to establish the SEEY magnitude. Anyway, an important aspect to be noticed is that the quantity of emitted secondary electrons is higher than the number of incoming primary electrons when the secondary electron yield coefficient exceeds unity. As the goal of the present work is to obtain enhanced values of plasma density, it would be convenient to achieve the highest SEEY as possible. Therefore, the secondary electron emission can be quantified by means of SEEY.

Given such considerations and relying chiefly on the value and trend of SEEY in function of the eV value, next Section will illustrate the research conducted for the selection of the most promising and feasible materials.

2.4 Selection of the Material

Previously it was introduced that, in plasma antenna applications, the principle on which the plasma source is based relies on the same working mechanism of CCFLs. Nevertheless, while the purpose of the latter is to emit light radiation, GPAs aim at signal transmission. In the present work both applications have in common the same commercial electrodes and share the same plasma generation mechanism. Therefore, it is reasonable to choose CCFLs as starting point for the material research.

2.4.1 MgO-coated Electrodes

As regards the lamps, the reference parameters are related to the emitted light, i.e. luminous efficiency and luminance. For the aims of this study, secondary electron emission was considered as well. In order to improve these aspects, one of the most mentioned material is magnesium oxide (MgO). Several tests were led to confirm the benefits obtained in terms of performance due to the addition of this compound. MgO coated Ni cup cathodes are used to improve the lumen efficiency of CCFLs. E-beam evaporated layers of magnesium oxide, which has a large secondary electron emission coefficient, can increase the lumen efficiency of CCFLs by 15-20% [34].

Lee et al [35], adopting MgO-coated electrodes, found in their experiments a reduction of both heat-generation at the electrode and ignition voltage and the increase of luminance and efficiency, in comparison with the conventional CCFLs. Figure 2.5 shows the lamp voltage and current with comparison between the reference lamps and the MgO-coated lamps of CCFLs. As the lamp current increases, the lamp voltage decreases due to the fact that the lamp resistance decreases with the increasing current. Nevertheless, the lamp voltage of MgO-coated CCFLs is lower than that of uncoated CCFLs. The decreasing rate of lamp voltage for MgO-coated CCFLs is about 5% lower than that of uncoated CCFLs. This results was predictable because of the high secondary electron emission of MgO-coated electrodes.

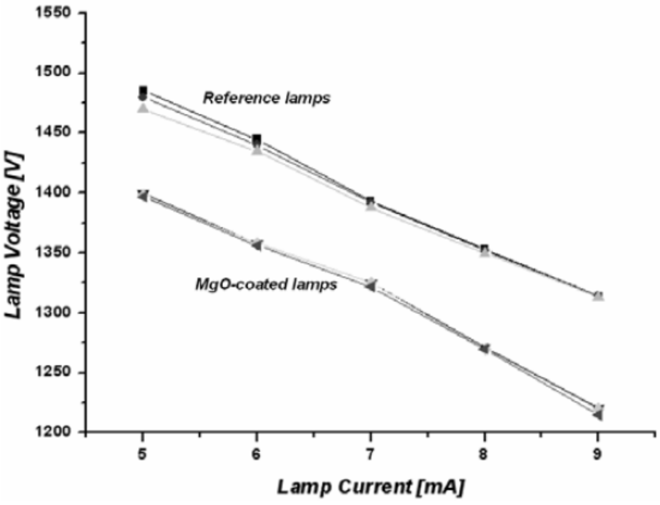

Figure 2.5: Lamp voltage versus lamp current with three reference lamps and MgO-coated lamps, respectively.

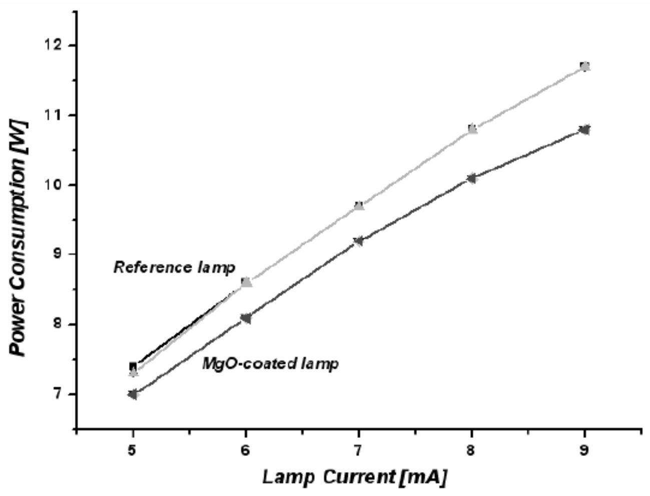

Figure 2.6: The power consumption versus the lamp current with the reference lamps and the MgO-coated lamps.

Figure 2.6 represents the results of luminance efficiency with the consumption power. The efficiency is increased by 5%. MgO has the effect to decrease the lamp voltage even if the lamp current and luminance values are kept the same.

2.4.2 The pellet-filled Hollow Cathode

The work presented in [36] shows an interesting idea in order to improve the performance of a cold cathode fluorescent lamp. The cathode fall in a low pressure gas discharge can be lowered by using cathode materials with a low work function. A way of dispensing a low work function material such as Ba constantly to the electrode surface is mounting a pellet containing a Ba-compound in a hollow cathode. During the normal operation of the CCFL the pellet at the bottom of the hollow cathode is constantly bombarded by positive ions and this leads to sputtering of Ba-atoms, which are deposited on the walls of the hollow cathode and lower the work function of the metal.

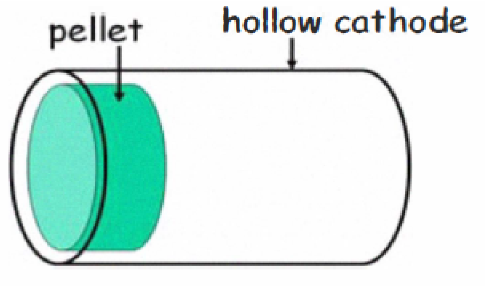

Figure 2.7: Hollow cathode with pellet containing a Ba compound.

According to [36] the cathode fall can even be reduced by bombarding the cathode surface with positive ions, thus increasing the secondary electron emission. The lumen efficacy of the CCFLs increased by 18% after coating the inner walls of a Ni-hollow cathode with a thin layer of MgO by e-beam evaporation. However, after 5000 hours of life test the lumen efficacy of the CCFLs with MgO-coated cathodes was equal to that of CCFLs with uncoated cathodes, which means that the MgO layer was removed by the phenomenon of sputtering.

2.4.3 Magnesium Oxide vs. Alumina and MgO+TiO$_2$

The aim of the experiments presented by *Jokela et al.* [37] is to determine optimal parameters for the deposition of secondary electron emissive materials, such as Al_2O_3 and MgO, as well as the development of material combinations which lead to enhanced SEYs.

The main goal is to determine an optimal film thickness for the secondary emissive Al_2O_3 and MgO coatings in order to set an upper limit to the necessary thickness of the secondary emissive coating required to achieve maximum SEY. MgO resulted to be a better secondary electron emitter than Al_2O_3, for which the maximum emission of 2.9 is achieved at a film thickness of 50 Å. On the other hand, as regards MgO films, the maximum SEY continues to increase with film thickness over the entire range of films, achieving a value of 6.9 for 200 Åfilms. Thicker MgO samples could not be examined due to sample charging, which occurs because of the increased distance electrons must travel from the conductive substrate to the origin of the secondary electron, resulting in a decreased SEY.

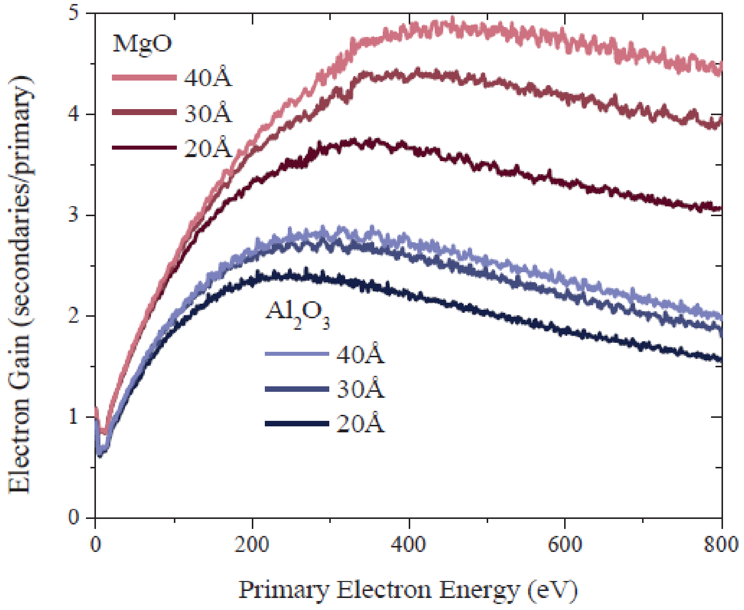

Figure 2.8: SEY for different thicknesses of MgO and Al_2O_3.

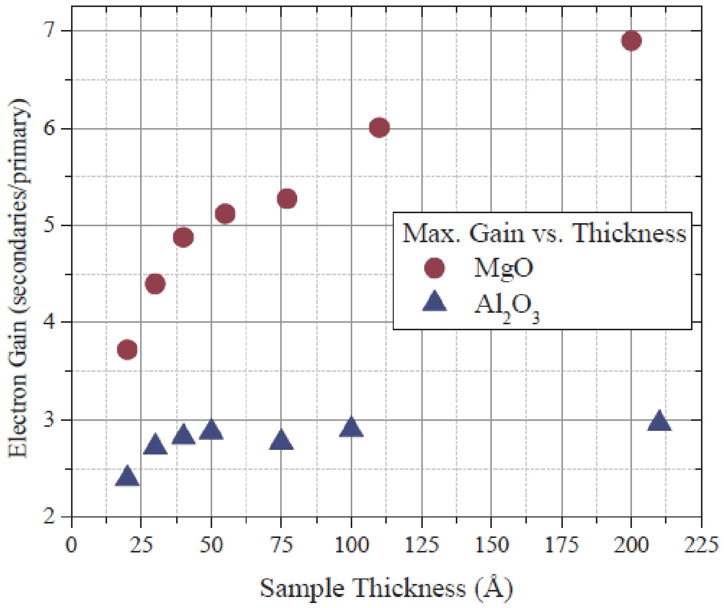

Figure 2.9: Maximum SEY vs. film thickness for MgO and Al_2O_3.

The samples were found to contain some amount of carbon on their surface, probably due to adsorbed atmospheric carbon. Al_2O_3 and MgO samples were measured before and after Ar^+ sputter removal of surface carbon. After Ar^+ sputtering, surprisingly, the SEY increased for MgO but decreased for Al_2O_3, possibly because the carbon compound on the material has a SEY greater than Al_2O_3 but lower than MgO, or maybe a different kind of bond between carbon and oxygen on the surface of the MgO sample formed a barrier for secondary electrons escaping the MgO surface.

The experiments in [37] proved that small amounts of TiO_2 added to MgO increased SEY from primary ions. Therefore, characterization of surface composition and the corresponding SEY were performed on four samples: MgO, MgO with the surface terminated in one monolayer of TiO_2, MgO/TiO_2 with 9 monolayers of MgO and 1 monolayer of TiO_2 repeating, and finally a sample of TiO_2. These samples were measured before and after Ar^+ sputtering. The Ar^+ sputtering caused an increase in SEY values for samples containing MgO, especially the MgO sample with the final surface layer of TiO_2. Quite the opposite, pure TiO_2 showed a decrease in SEY.

The ion sputtering not only removes the sample surface material, but it is able to mix surface atoms into underlying layers of the material as well. Indeed, some Ti was mixed within a few top-most layers of MgO, thus allowing it to act more as a dopant rather than an interface. Overall, the increase of the SEY caused by ion bombardment was sufficient to make Sample 2 an even more effective secondary electron emitter than pure MgO. In Sample 3 Ar^+ sputtering was apparently brief enough that most of the deeper Ti monolayers were left intact, hindering the emission of secondary electrons created deeper within the sample.

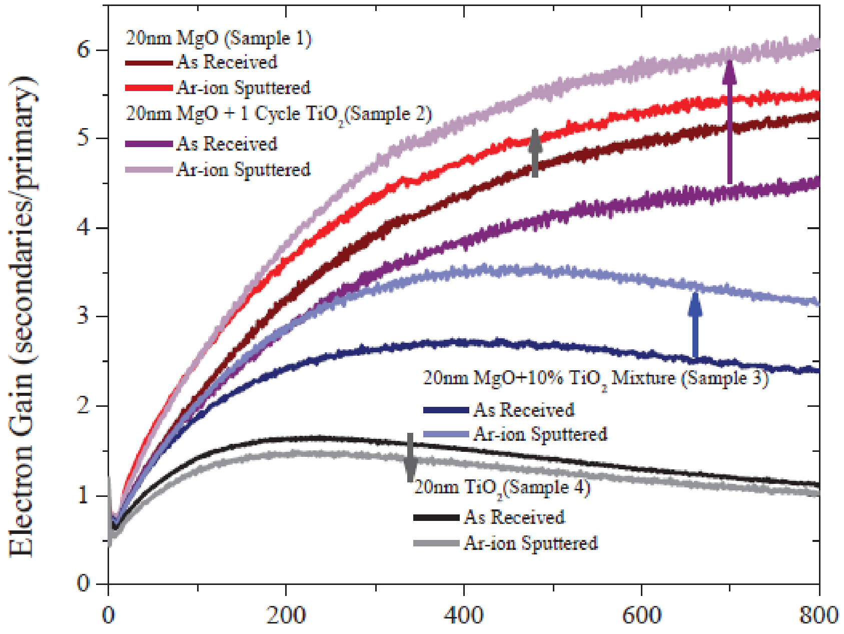

Figure 2.10: SEY for the four samples of MgO, TiO_2 and MgO combined with TiO_2.

2.4.4 CVD Diamond Films Coated with Alkali-halides

High secondary electron emission properties have been measured from CVD diamond terminated with hydrogen. The problems encountered using diamond as a secondary emitter are the instability of the secondary electron emission coefficient σ under electron beam exposure. Alkali-halides own electron transport and emission enhancing properties. The major drawback of using thick alkali-halide coatings in electron beam applications is their insulating property. However, thin alkali-halide films can be conductive.

In their work, *Mearini et al.* [38] used polycrystalline diamond films on Mo substrates grown by microwave plasma and hot filament assisted CVD, concentrating on CsI vapor deposited onto the diamond targets. σ versus time was measured from the CsI coated diamond films at room temperature and at temperatures up to 160^oC. The targets were exposed to the electron beam at current densities of 1.5–50.0 mA/cm^2, in a primary beam energy range of 1.0–1.5 keV, for durations of 6–170 h.

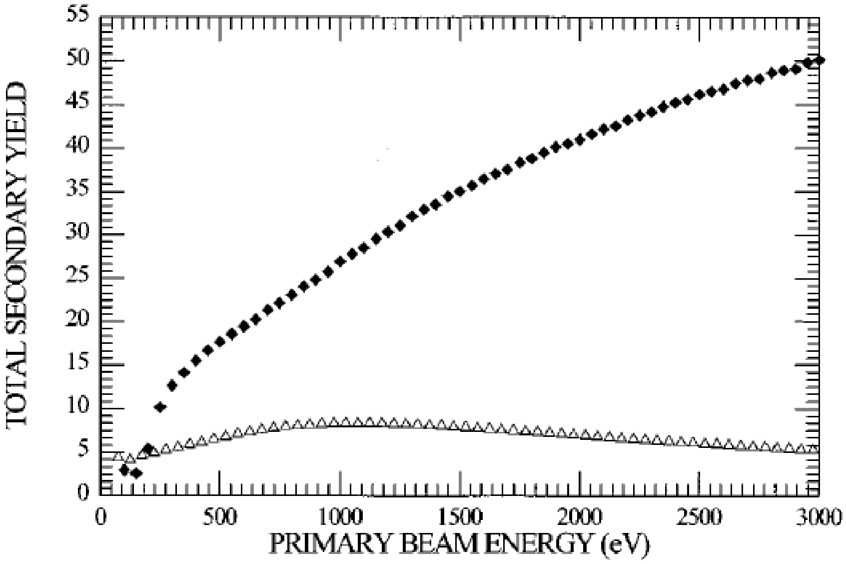

Figure 2.11: σ vs primary beam energy from a CVD diamond target before (△) and after (♦) deposition of a 10 nm thick CsI surface layer.

Maximum values of σ from the uncoated targets, at a beam energy of 1 keV, ranged from 6 to 12. Figure 2.11 shows σ versus energy before and after the deposition of a 10 nm CsI coating on the target. Figure 2.12 shows σ versus time from a 100 nm thick CsI film on Mo, and from a diamond target before and after a 10 nm thick CsI film was deposited. The value of σ from the uncoated diamond films generally degraded to ≈3 due to electron beam induced desorption of hydrogen.

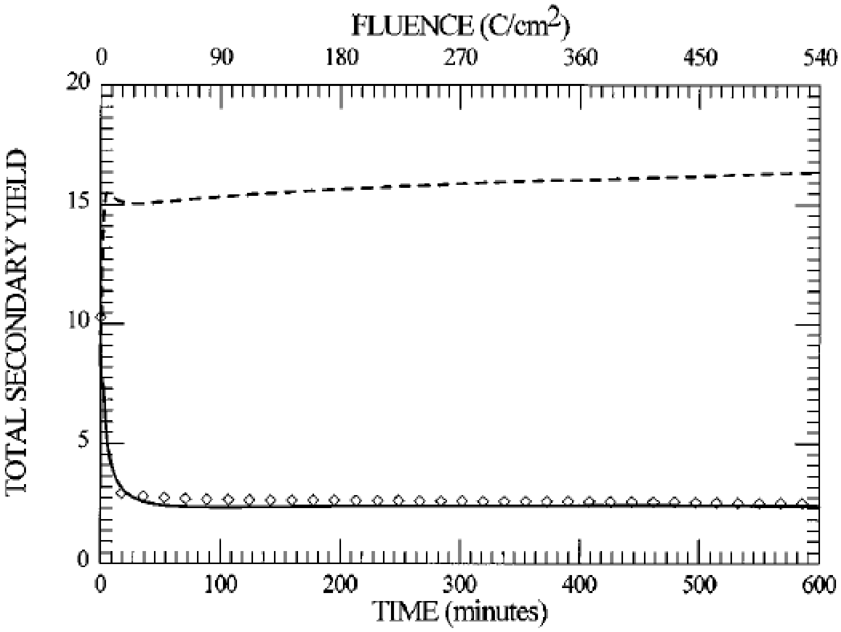

Figure 2.12: σ vs time from a CVD diamond target before (△) and after (dashed line) deposition of a 10 nm thick CsI surface layer. The solid line indicates σ from a 100 nm thick CsI film on Mo.

The value of σ from the CsI-coated diamond samples didn't show any sign of degradation, while in the coated samples in Figure 2.12 σ increased until the stabilization, after 67 h, at a value of about 22. All CsI-coated samples showed the same stable emission, regardless of the starting CsI coating thickness. Due to the continuous electron beam exposure, after relatively low fluences, the iodine was depleted leaving a Cs-rich diamond surface responsible for the high stable σ. Once the halogen has depleted, the electron beam activated-alkali terminated diamond films always exhibited a stable emission.

Despite the fluence necessary to activate the stable emission has proven to be dependent on the initial thicknesses of the alkali-halide films, on the other hand the final Cs concentration was independent of the initial CsI thickness. Even in the case of pure CsI on Mo the film was depleted of iodine due to the electron beam exposure, but σ saturated at a value of $\approx$3 [38].

2.5 Material Analysis Conclusions

The final goal of the present work is to reach a competitive design which optimizes both costs and performances. For this reason, even the cost of components and compounds as well as manufacturing costs played an important role in the material choice. Following the guide lines dictated by the compromise between these aspects and the results found in literature, the most logical conclusion led to the following possibilities:

- Magnesium Oxide (MgO): the simplest solution as it does not require the addition of other compounds;
- Titanium Oxide (Titania, TiO_2);
- Layers of $MgO + TiO_2$: the most promising possibility in terms of SEEY according to literature;
- MgO doped with small amounts of TiO_2;
- Aluminum Oxide (Alumina, Al_2O_3): this solution is as simple as magnesium oxide but it entails smaller values of SEEY.

A possible option which has been taken into consideration provided the substitution of both the commercial electrodes with two electrodes entirely made of molybdenum or nickel. However, despite its theoretical feasibility, this idea immediately encountered its descent due to the several problems involved. First of all, there was the necessity to design a new manufacturing process which required too much time for its development. Moreover, this aspect implicated a significant growth in terms of costs and complexity. For these reasons, this door has been left open for future developments and the choice went in the direction of coated electrodes by deposition of layers of MgO, TiO_2 or a combination of the two compounds via Sol-Gel method.

The reasons behind the choice of this process lie in its simplicity, cheapness, velocity and ease of monitoring. In addition, the sol-gel method requires low heat treatment temperatures (i.e. 500 °C), which are much lower than the glass softening temperature (i.e. 700 °C). The steps for the coating implementation will be presented in the following Chapter.

Finally, an experiment using a hollow cathode filled with a pallet will be carried on due to the theoretical simplicity of this idea in terms of costs, manufacturing and equipment required. Problems regarding this process are mainly the roughness of handmade pallets, the lack of practical test data and the variables related to the fixing between cathode and pallet. Despite these aspects, such an idea could lay the groundwork for bringing improvements to the process and take advantage of the phenomenon of sputtering in order to enhance secondary electron emission.

CHAPTER 3

Experimental Setup and Tests

3.1 Introduction

In this chapter test procedures and instrumentation will be introduced and described in detail. The reference parameter, measured to evaluate the plasma discharge performances, is the density. In the first part of this Chapter methodology and procedures will be presented and discussed, while the final part will be dedicated to the outcomes and results of data analysis in order to lay the foundation for future research and improvements.

3.2 Equipment

The whole bench equipment, developed by CISAS [39], consists of a power supply, a signal generator, a microwave interferometer, the connections with the PPU, probe and vessel. The PPU is a 2 stage transformer. Two bench power supplies are necessary to drive the set up properly as one of them provides stable voltage to the first stage of the PPU, while the second is used to tune the amplification stage. The two outputs of the latter are connected in series in order to allow for a dynamic range of approximately 60 V instead of 30 V. The signal generator is set on sine wave mode at a frequency of 910 kHz. However, this value can be tweaked to be as close as possible to the ideal condition of maximum power transfer.

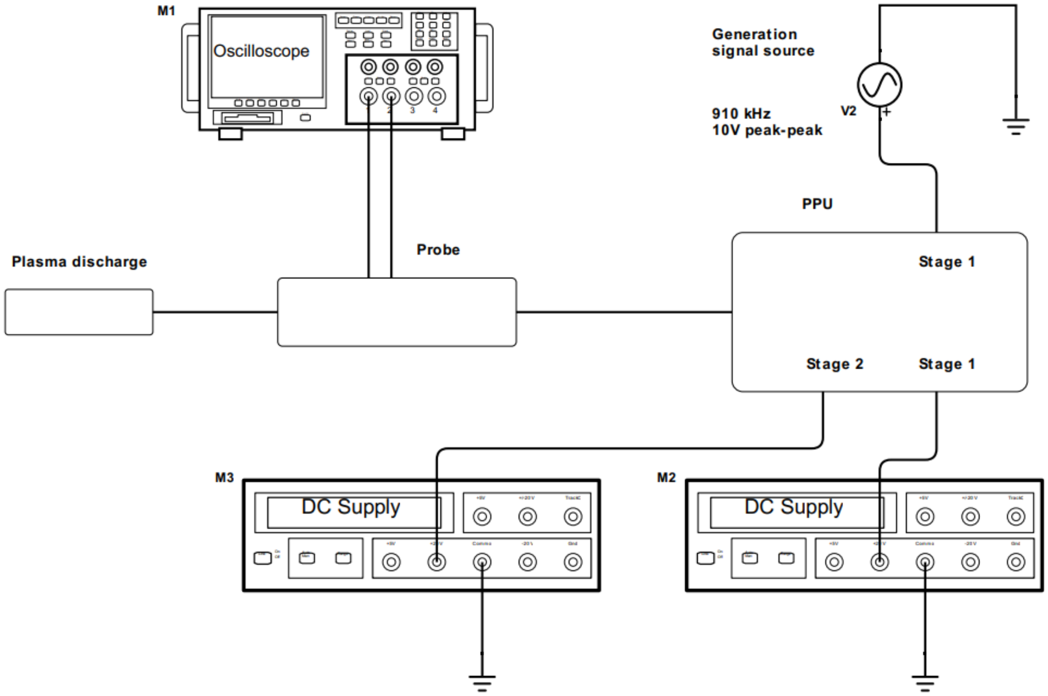

Figure 3.1: Measurement Setup

An alternative fixed point analysis setup, similar to the one shown in Figure 3.1, can be used. In this case, with one vessel only, the high frequency generator relies on a commercial high voltage transformer connected to two CCFL electrodes, contained at the extremities of the glass vessel. The transformer used for the experiments is a *MIDI ECG 2100* model Tecnolux (Figure 3.2), which turned out to absorb 30 W from the wall socket during testing. For the aim of this work, the first setup will be used for the tests.

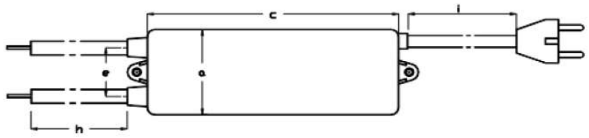

Parameter	Value
Input Voltage	200-250 V
Input Current	Up to 400 mA
Input Power	Up to 90 W
Input Frequency	50-60 Hz
Output Voltage	2 kV max
Output Short-circuit Current	95 mA
Output Current to Load	84 mA (nominal)
Output Frequency	19 kHz

Figure 3.2: MIDI EGG 2100 power supply and its techincal characteristics.

3.2.1 V-I Oscilloscope SIGLENT SDS1102 CML

Voltage-Current measurements are crucial to obtain a correct estimate of the power that is being delivered to the plasma. The two quantities are probed just before the connection with the electrode (after the PPU) and displayed on the channels of the oscilloscope (Figure 3.1).

Measurements are carried out in conjunction with the use of the interferometer, as it is interesting to link the power to the density value. This also implies that the waveform must be saved with accurate timing. The specifications of the instrument allow for precise sampling of the waveform without any aliasing or distortions, as both the rise time and sampling rate of this oscilloscope are much faster than the signal's variability.

Having an high input impedance, i.e. 1 $M\Omega$, is imperative for measuring devices. Nevertheless, it may create mismatches even if a matching adapter can be easily implemented in order to overcome this issue.

3.2.2 Phase Jump Interferometer

To fulfill the aim to measure the phase jump, it is necessary to make a phase comparison between a sample signal and the wave driven through the vessel. The instrument calibration takes into account the different length of the path but not the delay introduced by the plasma inside the vessel. Therefore, the phase difference can be used to estimate the electron density within the vessel.

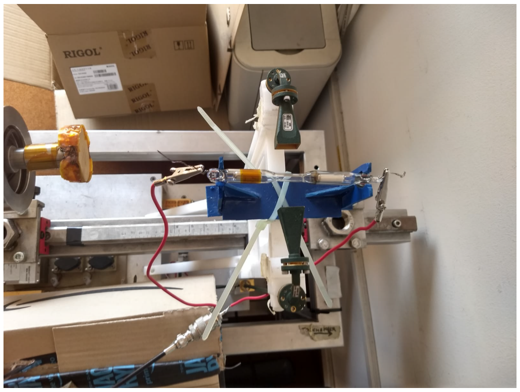

Figure 3.3: Vessel positioning (above)

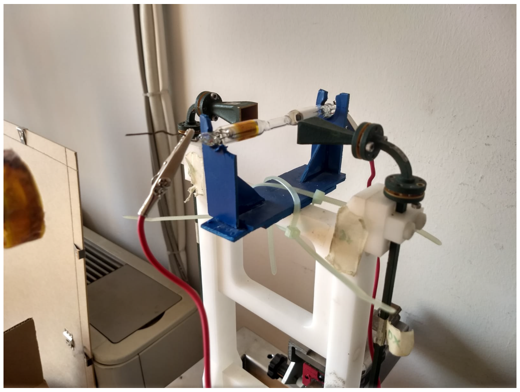

Figure 3.4: Vessel positioning (side)

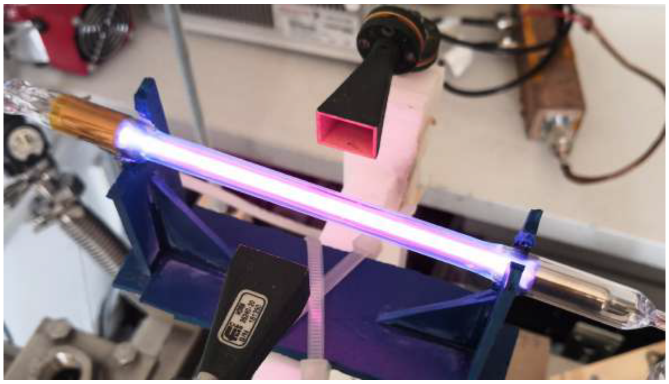

Figure 3.5: Vessel in the "on" mode.

Measurements can be launched by a dedicated PC, which runs the acquisition manager (Figure 3.6). The only values that need to be edited are the ones related to the acquisition time.

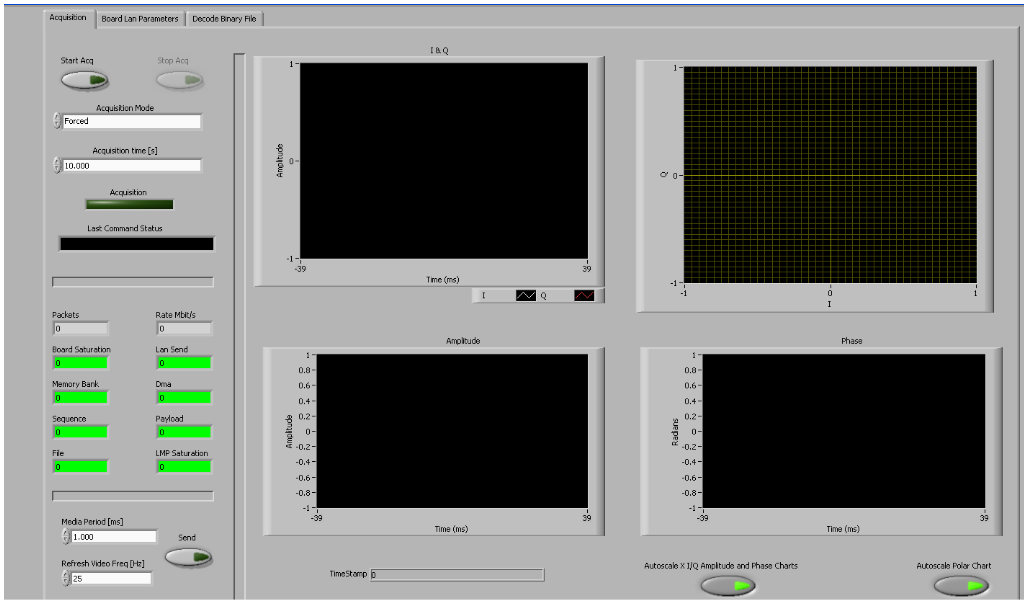

Acquisition Mode: Forced

Acquisition time [s]: 10.000

Packets: 0

Rate Mbit/s: 0

Board Saturation: 0

Lan Send: 0

Memory Bank: 0

Dma: 0

Sequence: 0

Payload: 0

File: 0

LMP Saturation: 0

Media Period [ms]: 1.000

Refresh Video Freq [Hz]: 25

TimeStamp: 0

Figure 3.6: Acquisition Manager

Measurements have to be launched manually by the user, while the end of the test is set automatically by the acquisition time value. Acquisitions are carried out using a phase comparator and the interferometer, which is set to a frequency of 75 GHz. At this working frequency, a noise contribution of 0.1^o will create a variation in density of $\approx 10^{16}\,\frac{particles}{m^3}$. On the other hand, a 2π phase shift (i.e. upper limit) is achieved when $N \approx 2.8 \cdot 10^{19}\,\frac{particles}{m^3}$. Therefore, the instrument is able to measure densities (in this configuration) up to $N \approx 1 \cdot 10^{19}\,\frac{particles}{m^3}$ with a 4 % error [39]. Because of the extreme sensitivity of the experiments to vibrations, the wave guides have been firmly secured to the support structure. Moreover, as vibrations introduce stray components above 100 Hz, post processing HF filtering smooths the spectrum.

This analysis underlines the role of precise phase difference acquisitions. In [39] it is explained that the phase jump generated by an unexpected temporal discontinuity in plasma density (i.e. turning on/off the discharge) can be linked numerically to said parameter.

3.3 Test Procedures

This section will outline the step by step procedure that has been followed for the measurements.

3.3.1 Density Measurements

These tests are usually performed at three points in voltage (i.e. 30, 40, and 50 V) as set on the power supply driving the amplification stage of the PPU (Figure 3.1).

1. The plasma discharge is carefully placed on the plastic support, paying attention to the position of the wave from the interferometer, which has to go through the centre of the vessel.
2. Crocodile clips from the MIDI ECG 2100 are connected to the wires protruding from the glass vessel. Even if polarity has not to be necessarily supervised, it is preferable to make the procedure the most repeatable as possible.
3. Turn on power supply 2 and set to the desired voltage.
4. Check if the voltage level is able to ignite the plasma by quickly enabling the output from the signal generator (should be appropriately set in advance). At this time is also beneficial to check the waveform on the oscilloscope because too much noise on the display may indicate an unstable connection.
5. Prepare the PC for the measurement, then enable the output from the signal generator. Otherwise, when performing the measurement the user must force a voltage spike and then lower the voltage in order to turn on the plasma.
6. Start the acquisition and after about 5 seconds, the waveform on the oscilloscope should be blocked and the output on the signal generator must be promptly disabled.
7. Save the output file from the interferometer through the acquisition program and store the oscilloscope data on a USB drive, then releasing the blocked display.

8. Turn the power supply off.

These test are usually performed over a time span of a few days. Furthermore for better accuracy each measurement is repeated 2 or 3 times.

3.3.2 Degradation Test

These tests have been designed to assess the performances of plasma discharges for longer ignitions. The density values are recorded both at the beginning and end of the measurements, so that they can be compared. The length of these tests can be set arbitrarily, depending on the needs and stability of the discharge itself. However 60, 90 and 120 seconds tests are the most common. For clarity and simplicity they will be addressed as degradation tests in the rest of this thesis. The detailed procedure follows below.

Steps 1-4 are equivalent to the ones outlined above. However test are performed at the maximum voltage available on power supply 2 (i.e. 60 V) only.

5. Start the acquisition from the PC.
6. After 5 seconds enable the output on the signal generator, promptly move to the oscilloscope, lock and save the data.
7. Release the oscilloscope display (Repeat steps 6 and 7 at the mid point in time for longer tests, i.e. 90 and 120 seconds).
8. 5 seconds before the end of the test lock the waveform again and quickly disable the output on the signal generator.
9. Save the data on the USB drive and export the data from the acquisition manager.
10. Turn off the power supply and carefully remove the vessel from the plastic support.

For easier understanding, a sketch of the timeline has been reported in Figure 3.7. It should be noted that the mid-point oscilloscope acquisition is skipped for 60 seconds tests.

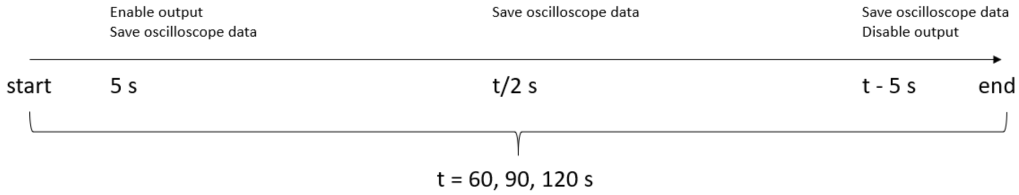

Figure 3.7: Timeline for Test Procedure

As mentioned before, an alternative procedure for the fixed point analysis with the MIDIECG 2010 exists. The only difference consists in avoiding the use of the oscilloscope and using the power supply socket switch instead of the signal generator to turn the discharge on and off.

3.3.3 Post-Processing

Data analysis has been performed by means of three MatLab scripts: *Interferometer_AmplitudeAndSlope.m*, *Oscilloscope_PPU_NewRigol_newPPU.m* and *plotData.m*. Even though all of these were already available, some modifications as well as improvements were necessary to adapt the scripts for different tests.

Interferometer_AmplitudeAndSlope.m was used to convert the phase data contained in the txt files from the interferometer into a density measurement as explained in [39]. Filtering the input data and implementing properly tuned conversion factors, statistical data can be extrapolated, thus resulting in a final matrix containing raw phase jump, maximum and minimum density, two uncertainty factors and density data. The script looks for the maximum value between the derivatives of the phase data and identifies the point in terms of time when the jump happens. Then the value of density is calculated as the difference in the phase between the points right before and immediately after the jump. Lastly, the final matrix is exported as *xls* file.

Oscilloscope_PPU_NewRigol_newPPU.m is used to process the oscilloscope files as saved on the USB drive directly (*csv* format) into an *xls* matrix containing the frequency, root mean square value of both voltage and current, the phase difference between voltage and current and the impedance.

PlotData.m must be launched as last, since it uses the outputs from both scripts as input and it plots relevant quantities. If measurement techniques vary the script probably requires some tweaking.

3.4 Size Comparison

In the present chapter the following notation will be used to describe the vessels: *TXXLYY*. This code identifies both the shell design and the length of the plasma column, with "*TXX*" describing the former while "*LYY*" the latter (in millimeters). The research has involved T7L40, T7L50, T10L50, T10L100 and T10L40 vessels.

The starting point of the research are Argon filled vessels, as they were the first custom-manufactured plasma discharges. They will be used as benchmark to evaluate the effects of different lengths and diameters of the vessels.

3.4.1 Density Measurements

Density tests are performed as explained in Section 3.3.1. Their main outcome is to evaluate the number of electron density within the vessel in terms of quantity, reliability and consistency with respect to the power applied to the PPU.

For this frst set of tests, 6 equivalent T10L40 vessels at 1.5 mbar of Argon were analyzed at three different power ratings, namely 30, 40 and 50 V as set on the power supply connected to stage 1 (Figure 3.1). The geometry is the one depicted in Figure 1.12. The following four plots report data from 5 consecutive test days, during which 2 measurements were taken each day. The studied discharges are marked with progressive numbers 1, 2, 5, 6 corresponding to the relative numbers written on the vessels.

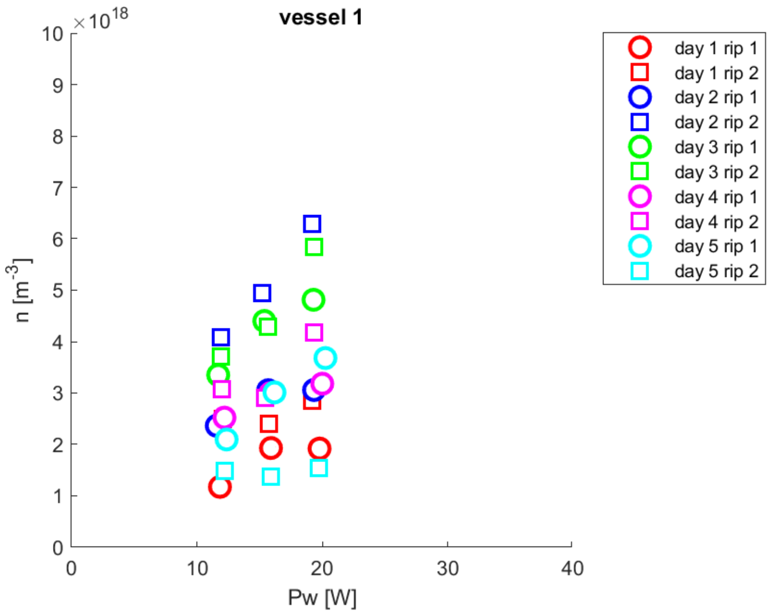

Figure 3.8: Benchmarking Tests - Density versus Power for Vessel 1.

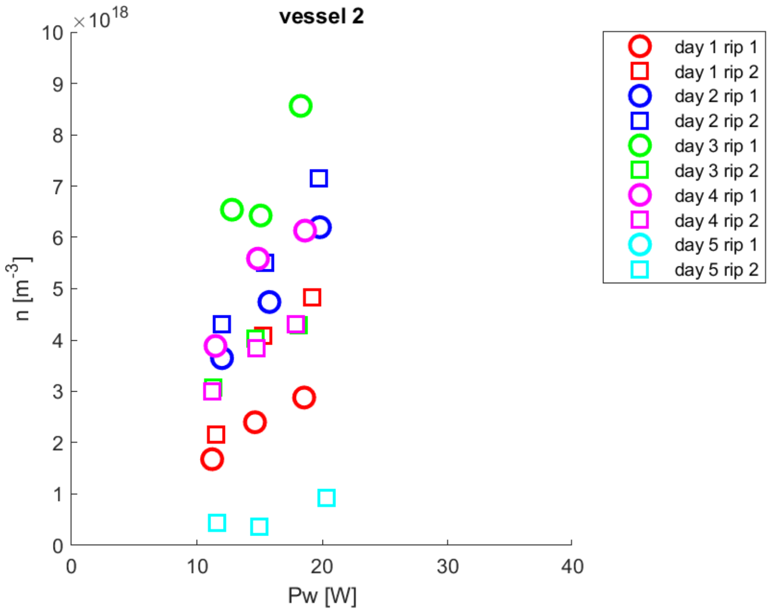

Figure 3.9: Benchmarking Tests - Density versus Power for Vessel 2.

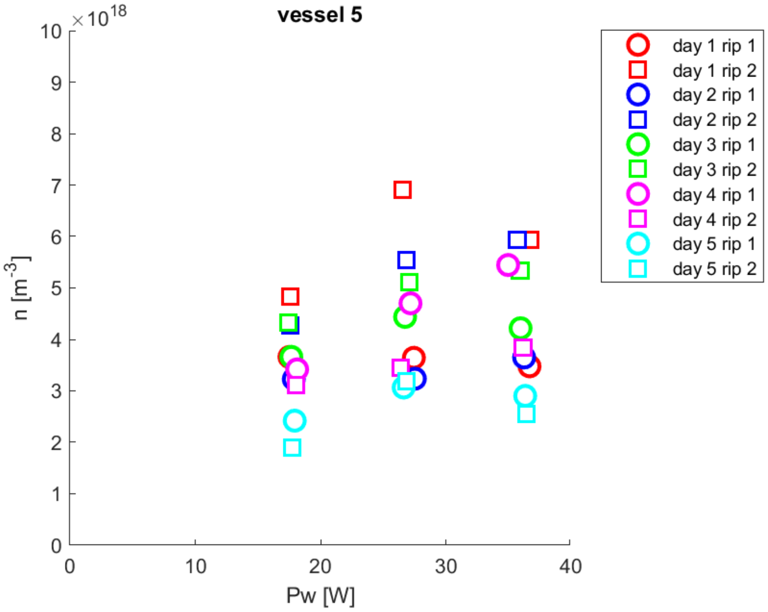

Figure 3.10: Benchmarking Tests - Density versus Power for Vessel 5.

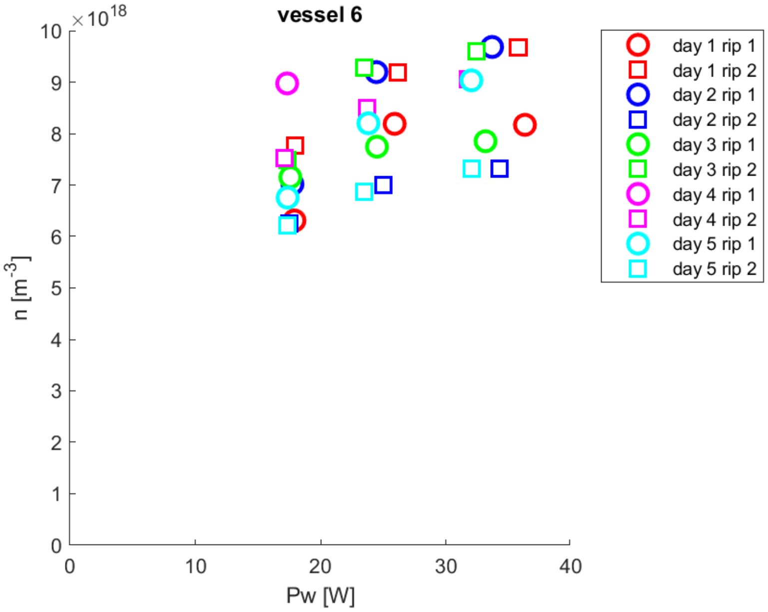

Figure 3.11: Benchmarking Tests - Density versus Power for Vessel 6.

Figures 3.8, 3.9, 3.10 and 3.11 show density measurement results for five-day benchmarking test on 4 T10L40 vessels. X-axis reports the coupled power, while Y-axis reports the density value. The density error related to these acquisitions is $\approx 10\%$.

As a general trend, all vessels show an increase in density for higher powers. However, no other noticeable common behavior is seen throughout the observation period. As a matter of fact, from the plots it is possible to grasp the high degree of variability that features plasma measurements among vessels whose characteristics are equal, i.e. all samples are T10L40 filled with Argon at 1.5 mbar. In particular, the power value is not consistent among all vessels, meaning that if the voltage is fixed the current draw varies, thus implying a difference in the impedance values of the discharges (see Figures 3.8 and 3.9 in contrast with Figures 3.10 and 3.11).

Figure 3.11 shows by far the best performances as density is always greater than $6 \cdot 10^{18}$, reaching values just below 10^{19}. Datapoints are also clustered together, meaning a great consistency and repeatability. Moreover, this sample showed a linear increase with the power. Considering the high variability of plasma measurements, these results are particularly remarkable.

Figures 3.8 and 3.9 indicate that vessel 1 and 2 should be discarded: the former shows poor performances with respect to number density as its maximum appears to be coincident with the minimum of vessel 6, while the latter is definitely not consistent and overall unreliable. It reaches the lowest point in density compared to all the other vessels as well. Figure 3.10 shows that vessel 5 does not perform well in terms of density, but its consistency is borderline acceptable. However, the relationship between density and power does not seems to be clearly linear especially on day one and day five.

More density tests were performed with the aim to compare different vessels in order to determine whether they had performances stable enough to move on to degradation tests. A total of six discharges were compared:

- T7L40 at 1.5 mbar (2x)
- T7L50 at 2mbar
- T10L40 at 2mbar (3x)

For simplicity only 3 results will be shown, one for each design, as to clarify how performances are assessed. Figure 3.12 reports the plot for T7L40 vessel 1, Figure 3.13 refers to T7L50 vessel 1 while Figure 3.14 reports the results for T10L40 vessel 3. Similarly to the conditions mentioned before, measurements were repeated for different voltage settings, i.e. 30, 40 and 50 V.

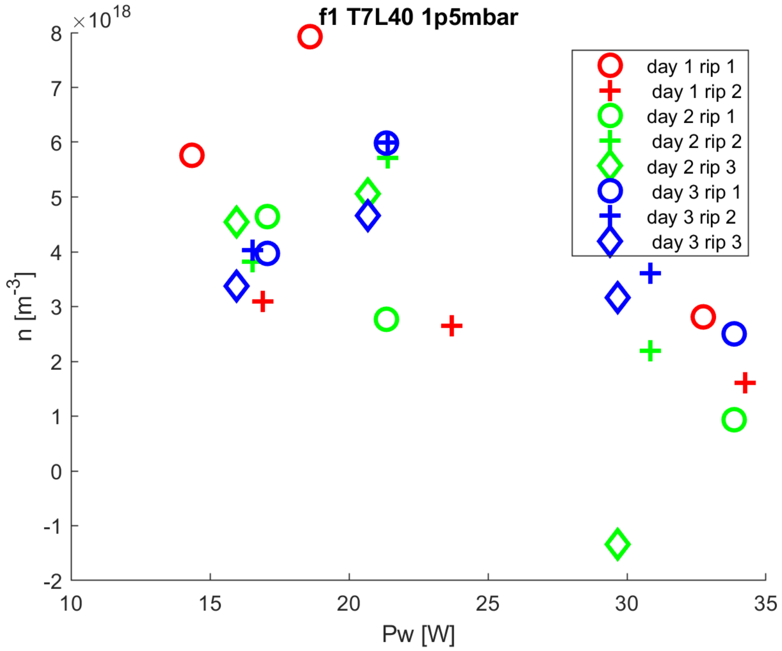

Figure 3.12: Density versus Power for T7L40 vessel 1 at 1.5 mbar.

In general, no distinguishable relationship between density and power can be observed throughout the plots in Figures 3.12, 3.13 and 3.14. However, the T10L40 vessel shows a remarkably linear trend. Power requirements differ among vessels as well, the only noticeable dissimilarity lies in the use of different electrodes, as the T10 cathode has a bigger diameter than the T7 electrode. Figures 3.12 and 3.13 show that T7-type electrodes are not capable of sustaining a stable plasma, considering that all the data point are scattered in the graph. All the 3 T10L40 vessels behave similarly and the one reported in Figure 3.14 performs the best results, as none of the others attains similar density values.

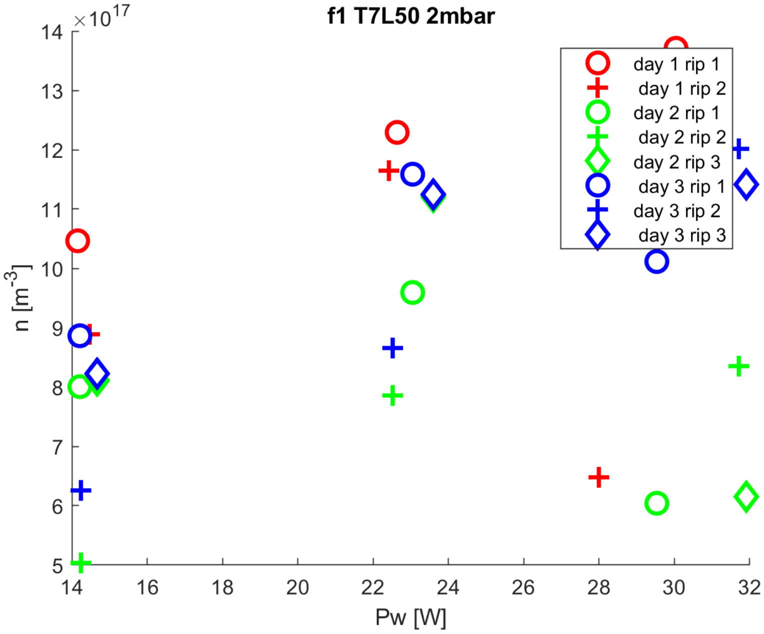

Figure 3.13: Density versus Power for T7L50 vessel 1 at 2 mbar.

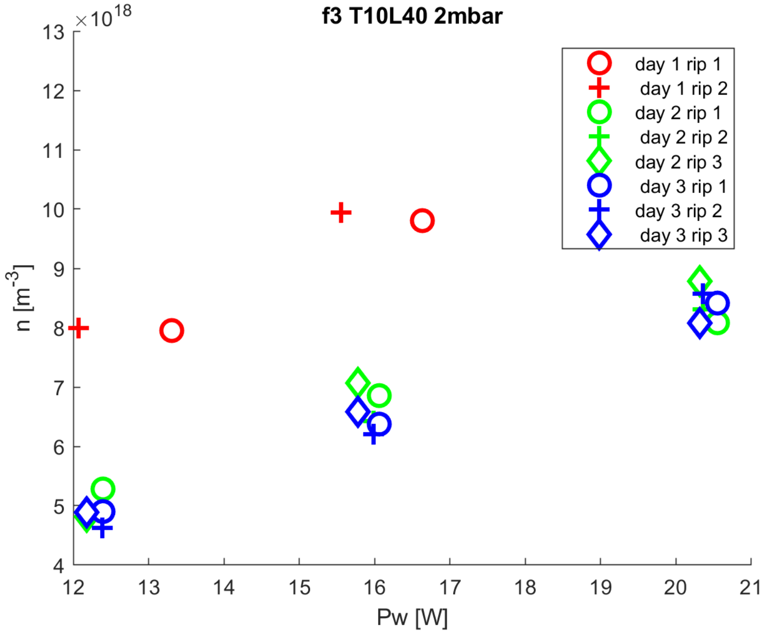

Figure 3.14: Density versus Power for T10L40 vessel 3 at 2 mbar.

Furthermore, after day one the points appeared already stabilized on a consistent remarkable density, reaching values up to $9 \cdot 10^{18}$. From such results the obvious conclusion is that only T10L40 vessels were good candidates for a longer tests, useful to assess degradation, since their density was found to be consistent over multiple shorter tests.

Vessel	30 V	40 V	50 V
f1T7L40 1p5 mbar	1.69	1.52	1.81
f1T7L50 2 mbar	0.20	0.17	0.20
f3T10L40 2 mbar	0.18/0.12	0.16/0.10	0.19/0.12

Table 3.1: Deviation from mean value (divided by 10^{18}) verifying the reliability of T10L40 discharges. The third row reports two values corresponding to different sample choices.

The just mentioned analysis is even confirmed by the data in Table 3.1, where the deviation from the average trend is reported. It clearly shows the high reliability of the T10L40 vessel, since its values are consistently lower.

The averaging samples are chosen carefully using the values on which the vessel has stabilized and eliminating day one samples, thus the deviation is further reduced. This aspect can be observed in the last row of Table 3.1, where the data after the backslash is yielded with the latter assumption. This choice was led by the trend in Figure 3.14, where the density at day one was significantly different from the rather consistent values recorded during the following days.

Such low reliability is due to an undesirable level of control and precision over the manufacturing process itself. As a matter of fact, dielectric deposition of the metallic shells is an unknown variable and its distribution is usually highly non-uniform. This translates in great variability both among plasma discharges as well as different measurements of the same vessel. There are ongoing studies related to the optimization of such process but they are our of the scope of this thesis.

3.4.2 Degradation Tests

Depending on the outcome of the density measurements, the vessels that were found to be more stable and reliable were used for longer tests in order to assess their performances and endurance. The aim of these acquisitions was to compare the electron density value and the interferometer plot for different time frames. Therefore, one of the scopes of the comparative study described above was to make a preliminary step in order to narrow down a selection of discharges that have fairly stable density values.

To summarize, three T10L40 vessels (numbered sequentially 1, 2 and 3) with a nominal pressure of 2 mbar were tested at the maximum voltage setting, i.e. 50 V on the stage 1 power supply. However, considering the qualitative scope of this tests, only one discharge will be taken into consideration, namely vessel number 3 T10L40, whose performances have been assessed and evaluated in the analysis described above.

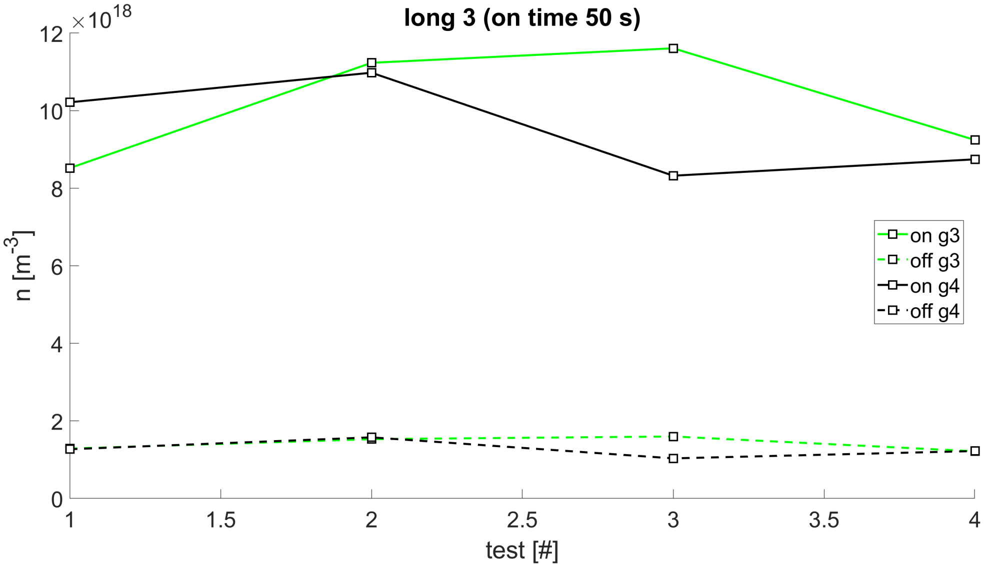

Figure 3.15: Comparison for a 60 seconds degradation test performed on vessel 3 T10L40 at 2 mbar twice per day for a two-day test session. X-axis reports the progressive test number, Y-axis reports the density value. Measurement error on the density of $\approx 10\%$.

The plots in Figure 3.15 shows the density values across different days both for the on (≈ 5 s) and off (≈ t - 5 s) jump allowing for a comprehensive understanding of the behaviour of the discharge.

Given the differences in density values at the beginning and at the end of the test, as can be seen through the gaps between dashed and solid lines of the same colour in Figure 3.15, the next step was to examine the phase behaviour directly. Considering that the trends and values for the three vessels are similar, the following analysis has been conducted on one single specimen, namely vessel 3 T10L40 at 2 mbar of pressure in Argon.

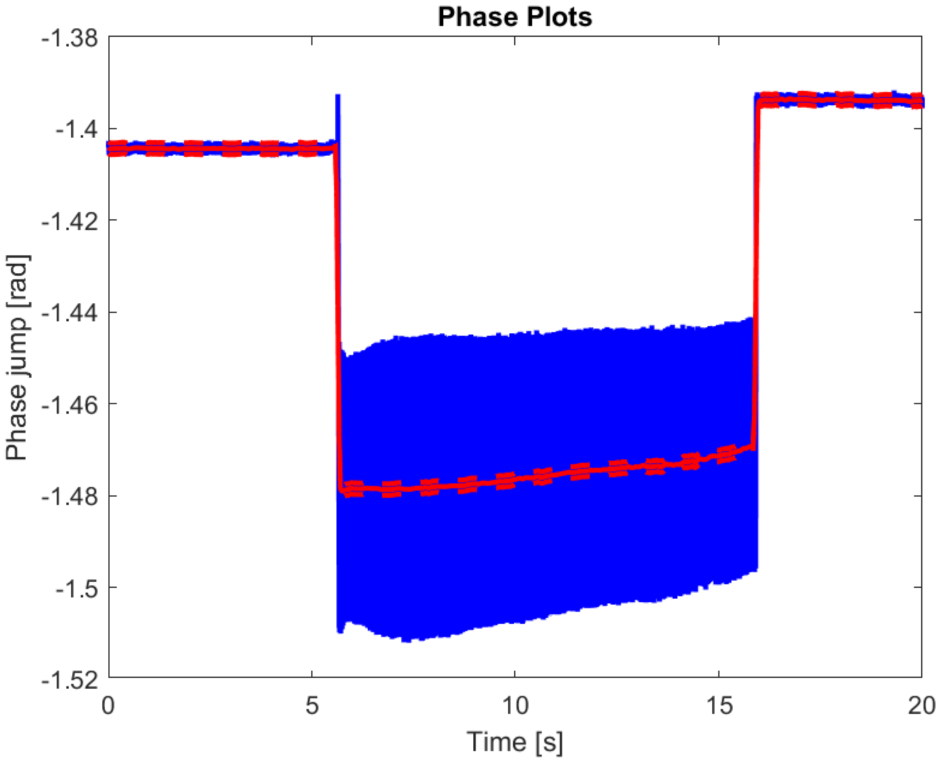

Figure 3.16: Phase plot for a 20 seconds benchmarking.

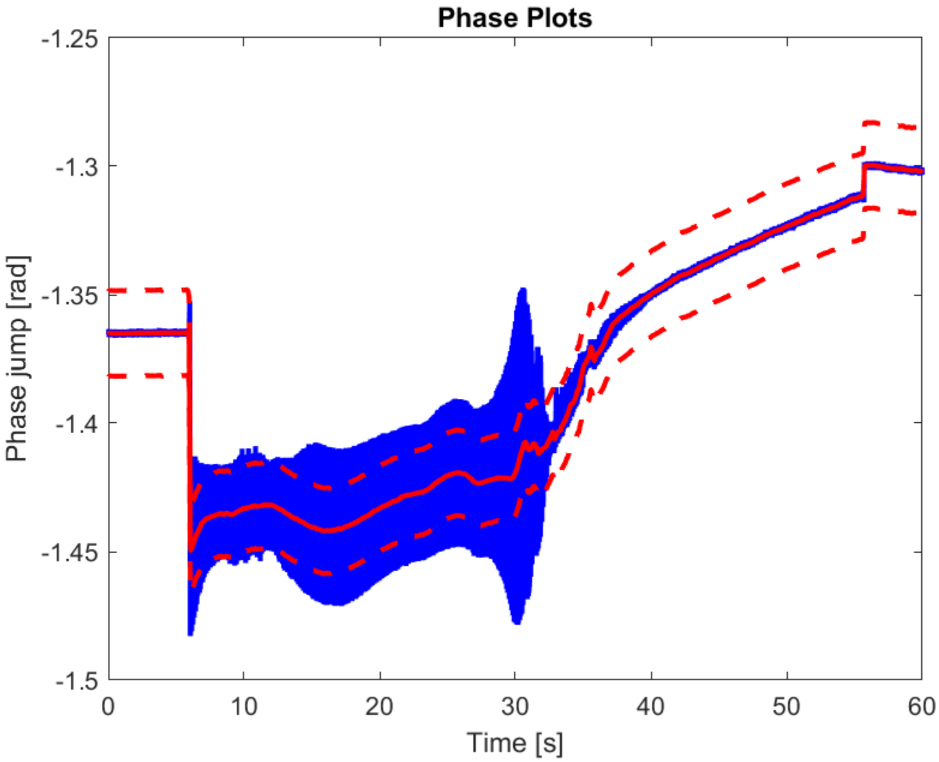

Figure 3.17: Phase plot for a 60 seconds degradation test.

After the analysis of the phase plots in Figures 3.16 and 3.17, a common trend was spotted, namely a noticeable change in the slope of the trace (Figure 3.17) after around 35 seconds from the start of the test despite the length. Interestingly, the slope appeared to drop to its initial value in less than 10 seconds.

Figure 3.16 reports a phase plot for a 20 seconds spark and used to verify whether the discharge has undergone severe damage during testing. On the other hand, Figure 3.17 shows the trend of the phase for a 60 seconds degradation measurement. Similar behaviour was observed for 90-second tests as well. This aspect suggested the idea of comparing the slopes before and after the increase had taken place.

This time spans are roughly constant across the measurements, however they vary depending on the test length. Therefore, examples for the three different duration will be reported. The script created to process the data performs linear interpolation according to the delimiters set by the user. The projection is then used to assess whether or not the difference in the slope is caused by plasma instabilities or other factors.

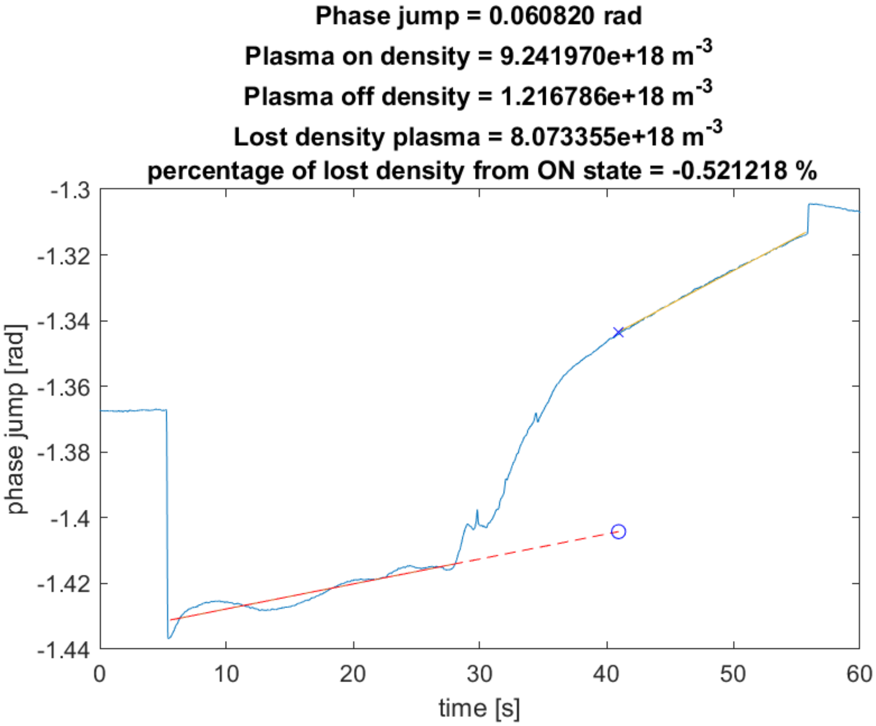

Figure 3.18: Interpolation for a 60 seconds test on vessel 3 T10L40 for a qualitative assessment of the degradation impact on the density.

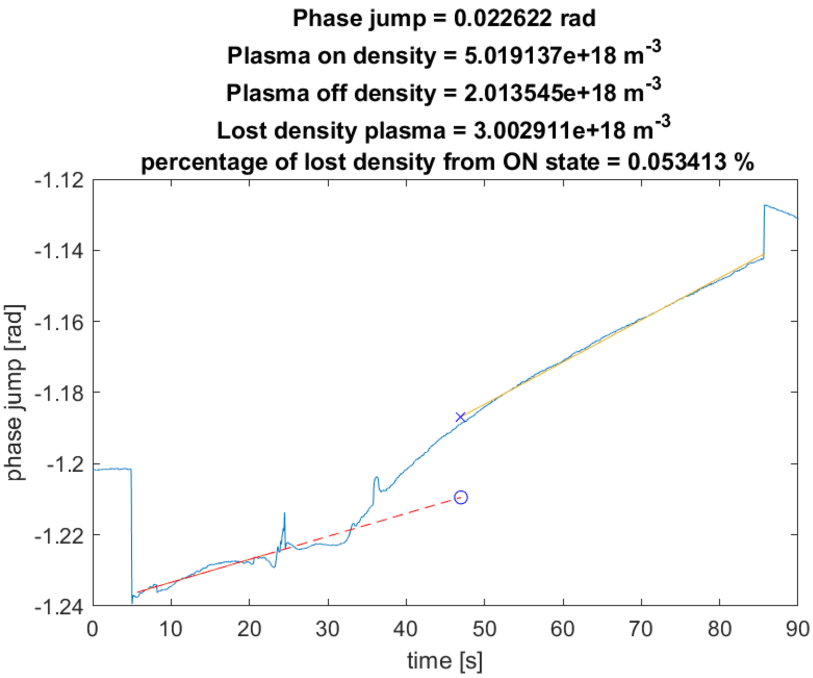

Figure 3.19: Interpolation for a 90 seconds test on vessel 3 T10L40 for a qualitative assessment of the degradation impact on the density.

Even though these test do not show ground breaking results, they are really useful to have a better idea of how the plasma behaves for longer ignitions time spans. Conclusively, the plots only show that degradation in performance takes places in the same time span, regardless of the test length. This can be understood by calculating the density value associated to the steep slope portion of the graph and verifying that, once added to the final density value, it roughly sums up to the initial electron number provided that the interpolation points are chosen carefully. The remaining drift in the density value could then be associated with the glass enclosure expanding due to heating stress.

It is important to point out that this behaviour has appeared to be reliable, as this phenomenon happened in every long measurement, meaning that such degradation process is not irreversible. A possible conclusion is that the high temperatures reached during long degradation tests severely hinder the secondary electron emission from the material deposited on the shells.

CHAPTER 4

Deposition Method

4.1 Introduction

In the previous Chapter it has been proven that T7-type electrodes are not capable of sustaining a stable plasma, while T10 electrodes, having a bigger diameter than the former, have shown much more stable plots and consistent density values throughout the measurements. Therefore, T10 electrodes will be used as samples for deposition tests. The present Chapter aim, indeed, is to describe the deposition methods and their application on some specimens.

Two deposition methods have been chosen to perform such tests: the sol-gel method and the deposition by sputtering of a pellet fixed at the end of a hollow cathode. The Sol-Gel method was considered the most suitable in order to reach this goal as it allows to obtain the required coating rather cheaply and quickly. The last section of the Chapter will show some results from tests on coated electrodes.

As just mentioned, the core of this Chapter will show the procedures implemented for the realization of the films. In addition, the optimization and improvement of each step will be described as well. The Sol-Gel technique represents one of the most studied and employed methods to obtain high quality ceramic materials ([40] [41] [42]). Nevertheless, there is no evidence about the use of this technique in the current application. This means that it will be necessary to verify its suitability for the purpose of this study. An aspect which is worth highlighting is that the choice of a method rather than another, in a given working condition, could affect the material yield.

These experiments were carried out at the University of Padova laboratory, since chemical processes were involved.

4.2 The Sol-Gel Process

The sol-gel method is a widespread technique used to obtain vitreous and ceramic materials. The first part of the process involves the conversion of monomers into a colloidal solution (sol), which then acts as a precursor for an integrated network (gel) of either polymers or discrete particles. A "sol" is defined as a stable suspension of colloidal solid particles within a liquid, where colloidal system stands for a mixture in which a matter is microscopically dispersed. A "gel", instead, can be described as a porous three-dimensionally interconnected solid system which expands in a stable fashion throughout a liquid medium. The nature of gels depends on the coexistence between the solid and the liquid medium.

The next phase of the process is the gelation. A gel is generated from the hardening of the homogenous dispersion present in the initial sol. The gelation prevents the development of inhomogeneities within the material. At the gel-point the sol sharply changes from a viscous liquid state into a solid phase called "gel" [41].

The great advantages of the sol-gel method are its cheapness and the low-temperature approach which allows the control of the product in terms of chemical composition. Moreover, compared to traditional techniques, this process shows high versatility and ease of monitoring as well. In addition, the sol-gel method allows the production of new hybrid organic-inorganic materials which do not exist in nature. In the sol-gel technique, the chemical processes of the first steps are always carried out at room temperature and chemical interactions between the material and the container walls are considerably reduced if compared to conventional ceramics [41].

Furthermore, the size of the particles of sol-gel ceramics can be easily controlled. An amorphous or semi-vitreous state is, for example, quite easy to obtain and many types of glasses that were not feasible by the conventional processes can be synthesized. On the other hand, the sol-gel synthesis of ceramics is not able to compete for mass production of large scale materials for which the conventional processes can depend on much cheaper raw materials.

Being a very widespread and applied process, the sol-gel technique owns many definitions and designate a large variety of procedures. For the aim of this work, the sol-gel process will be defined as a colloidal system employed to synthesize ceramics with an intermediate stage including a sol and a gel state. However, it is possible to bring many variations to the sol-gel synthesis of ceramics. [41]. Overall, the process is obtained following three main steps:

- Precursors selection of the chosen material. The chemistry of the precursor guides the reaction towards the formation of either polymeric gels or colloidal particles.
- Creation of a solvent-precursor mixture, with the resulting solution transforming into the gel.
- Heat treatment of the gel in order to attain the searched compound. To obtain a compact mixture, this final step is necessary as it removes the residual solvent allowing for material crystallization.

4.3 Deposition of MgO

Manufacturing processes finalized to the coating of metallic surfaces have never been realized for the present application. Therefore, several attempts have been made before the procedure could be optimized. The process has been developed with the aim to obtain the best possible results with great affordability and easy repeatability. In the previous chapters it came out that magnesium oxide is one of the most widespread and promising materials in terms of secondary emission. Moreover, MgO greatly matched the need for a cheap and available raw material, thus the process has been developed using the magnesium oxide using cylindrical glass tubes as samples.

According to the work presented in [43], the preparation of the compound, in this case a 25% wt solution, by mixing solvent and precursor is the first step. The precursor used for the creation of MgO coating was magnesium ethoxide (granular, purity $\geq$ 98%), dissolved in 2-methoxyethanol (anhydrous, purity $\geq$ 99.8%). Successively, the obtained mixture is stirred for two hours by means of a magnetic-stirrer. Such deposition method is the cheapest and easiest one. Finally, the following samples have been prepared:

- sample filled with the solution, shaken for a few seconds, then voided and dried at room temperature overnight;
- sample filled with the solution, shaken for a few seconds, then voided and dried at 75^{o}C in oven overnight;
- sample filled with the solution, left at rest (filled) at room temperature overnight;
- sample filled with the solution, left at rest (filled) at 75^{o}C in oven overnight.

Figure 4.1: Cylindrical glass tubes prepared for MgO sol-gel coating.

During the drying process, the sol-gel solution undergoes hydrolysis. Finally, the specimens are treated at a curing temperature of 500^{o}C in air, with a heating ramp of 10^o/min. Successively, the temperature is set still for one hour and in the end gradually decreases with another ramp of 10^o/min. After the procedure is completed, the formation of MgO on the glass surface occurs.

Figure 4.2: Picture of the oven for the heat treatment with ramp.

Scanning Elctron Microscope (SEM) images, made by *JSM Jeol 6490* SEM model at the CEASC of University of Padova, have been used to verify the deposited coating conditions. In Figures 4.3 and 4.4 the morphology and thickness of the layers were investigated and MgO crystals can be clearly observed.

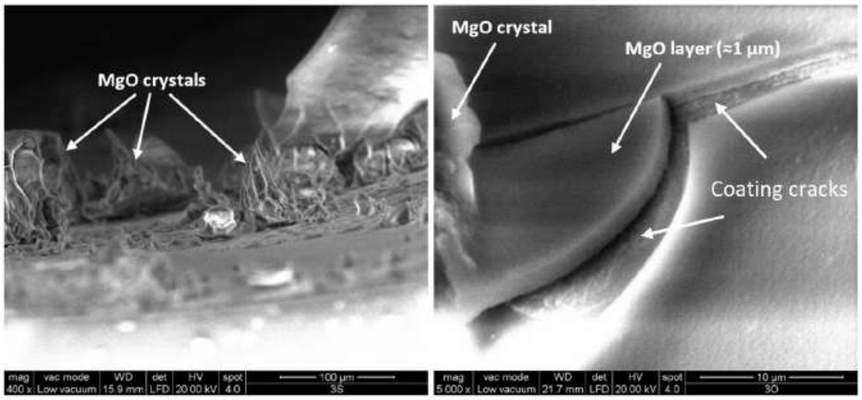

Figure 4.3: SEM images of MgO crystals and layer on glass substrate.

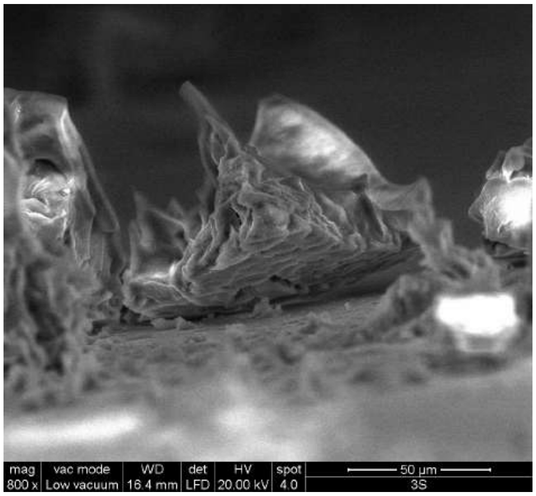

Figure 4.4: SEM image of MgO crystals with focus on the raised layer from the substrate.

The final heat treatment leads to the crystallization of the material by means of the evaporation of residual solvent. It should be noticed that the drying process heavily affects the characteristics of the final solution, defining changes in its homogeneity and porosity. In Figures 4.3 and 4.4 it is clearly visible the non-uniformity and irregularity of the deposited film, with the presence of evident cracks and parts of the coating raised from the substrate as well. This means that the deposited layer has not adhered properly. The development of cracks is most likely to occur precisely during the drying phase. This phenomenon may be caused by the fact that bigger pores dry quicker than smaller ones due to the higher vapour pressure of the liquid, thus introducing residual stresses. Moreover, another cause which probably explains the high presence of cracks on the coated film is that the weight percentage used to create the solution is not appropriate. Therefore, a 5 % wt mixture has been prepared. In addition, a chemical functionalization of the surface has been performed in order to enhance the adhesion properties of the deposited layer. Indeed, the surface functionalization aims to modify its chemical composition by integrating functional groups. For this scope, a solution known as basic Piranha has been applied to achieve a chemical attack. Such solution is composed of a strongly oxidising reagent ammonia, NH_3 25 % in aqueous solution, and hydrogen peroxide, H_2O_2 40 % in aqueous solution.

A further attempt to improve the process was made in the direction of enhancing the surface wettability. Thus, each sample underwent a 20-minute immersion at a temperature of 70^{o}C over a hot-plate. Samples were left in a container filled with distilled water until use and then dried with a compressed air jet. Successively, the 5 % wt solution has been prepared and the specimens have been coated, repeating the cases previously mentioned.

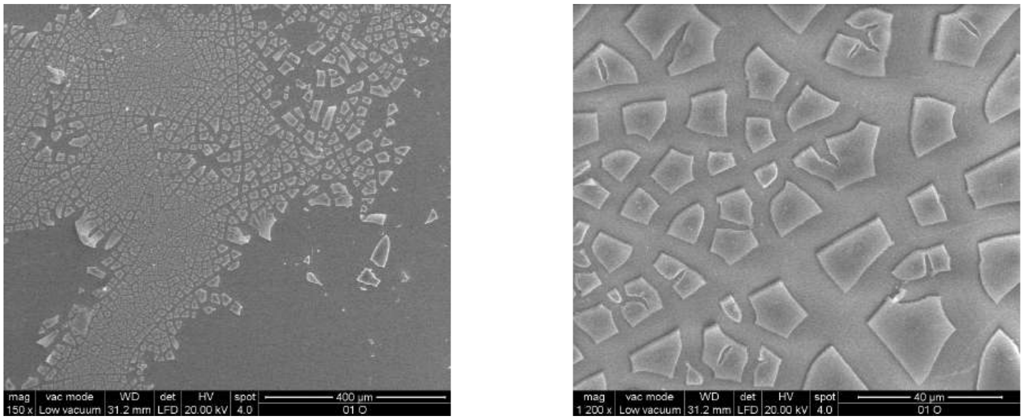

Figure 4.5: SEM images of MgO coating with 5% wt solution after the use of piranha solution.

The SEM Figure 4.5 shows that the central region of the coating has properly adhered (darker area). Unfortunately, still many cracks are present and the layer is not uniform.

As regards the improvement of the morphology, the *dip coating method* was implemented. Such process is helpful to generate thin films over a solid substrate by the immersion in a phial containing the liquid solution, thus allowing the production of several layers with different thickness as well. This step is followed by sample drying. The dip coating method involves the use of the dedicated device shown in Figure 4.6, which works in a humidity-controlled environment. Samples are fixed to a support moved by a piston (Figure 4.7), which velocity is remotely controlled by the user. Homogeneous deposited films can be generated simply by setting a fixed immersion and comeback velocity. The thickness of the coated layers is supposed to be constant throughout the specimen.

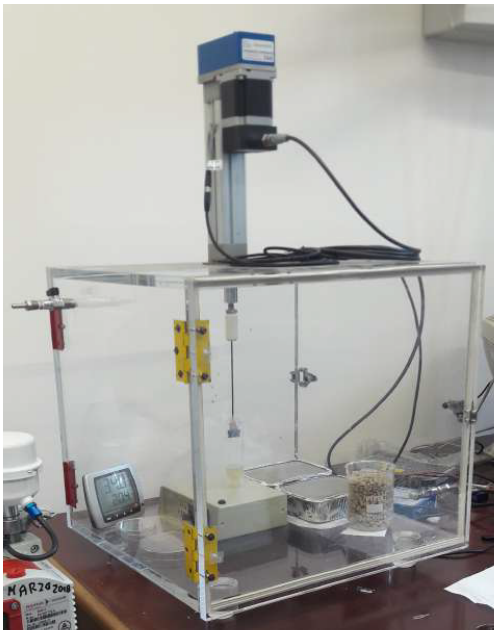

Figure 4.6: Equipment for dip-coating deposition method.

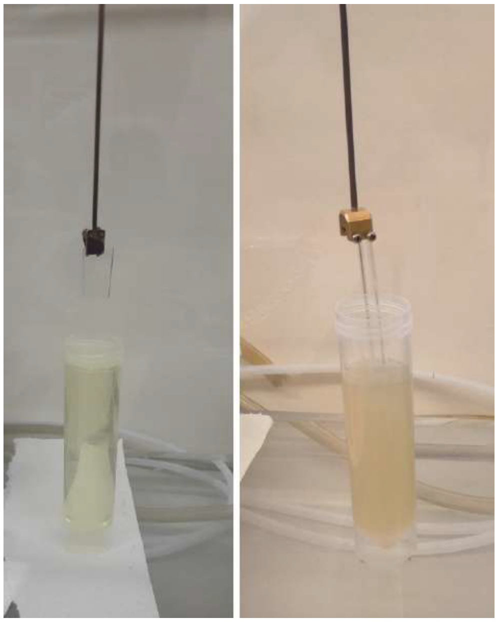

Figure 4.7: Support for specimens during dip-coating process.

In order to better investigate the exact value of the deposited layer thickness, samples were analysed by means of a *KLA-Tencor P-16+* contact profilometer, which uses a diamond stylus pressed on the sample and moved along a direction for a specified distance. This device can measure even small variations detected by the stylus along the vertical direction, which are directly related to the surface morphology of the specimen. Profilometer scans can be 200 mm long and own a vertical resolution of few nanometres. This time the coating has been deposited over a slide made of soda-lime glass because of the difficulty to perform the analysis on the inner walls of coated cylindrical glass tubes. Tests were conducted using three different velocities, i.e. 10 cm/min, 20 cm/min and 40 cm/min, as shown in the Figures below.

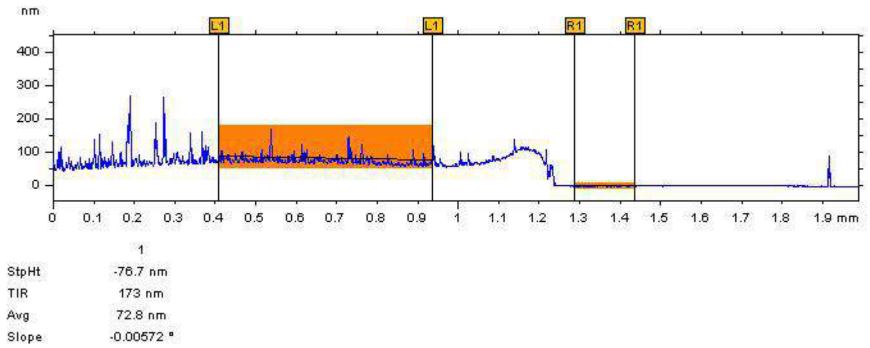

```
            1
StpHt    -76.7 nm
TIR       173 nm
Avg       72.8 nm
Slope    -0.00572 °
```

Figure 4.8: Profilometer result for dipping velocity of 10 cm/min. MgO layer thickness = 76.7 nm.

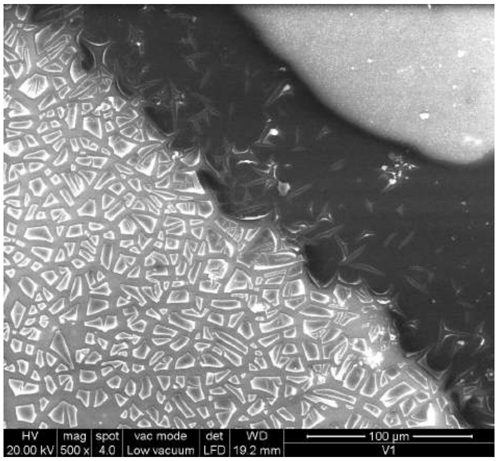

Figure 4.9: SEM image of MgO coating for dipping velocity of 10 cm/min.

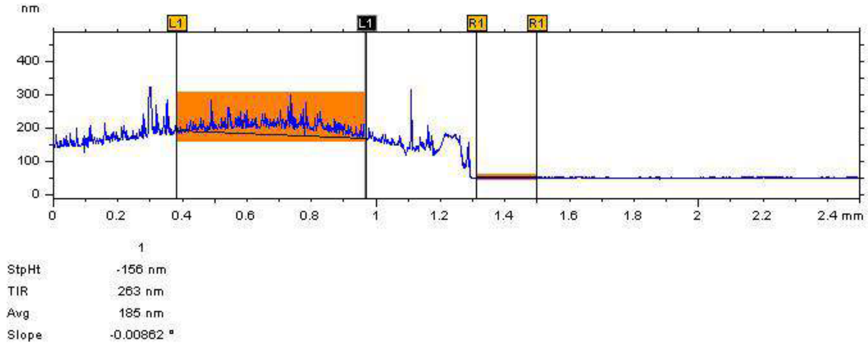

	1
StpHt	-156 nm
TIR	263 nm
Avg	185 nm
Slope	-0.00862 °

Figure 4.10: Profilometer result for dipping velocity of 20 cm/min. MgO layer thickness = 156 nm.

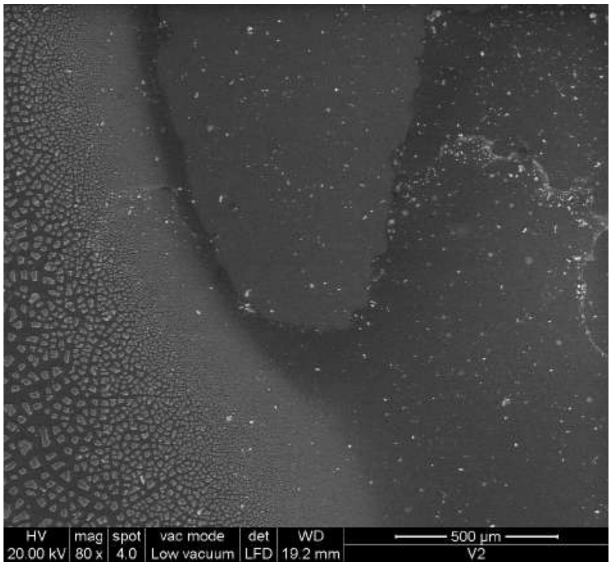

Figure 4.11: SEM image of MgO coating for dipping velocity of 20 cm/min.

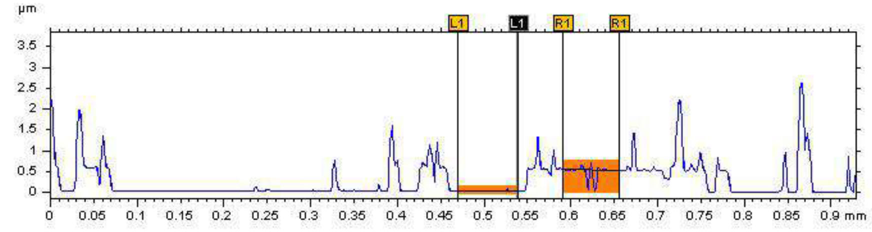

```
               1
StpHt      0.469 µm
TIR         1.31 µm
Avg        0.247 µm
Slope       0.249 °
```

Figure 4.12: Profilometer result for dipping velocity of 40 cm/min. MgO layer thickness = 470 nm.

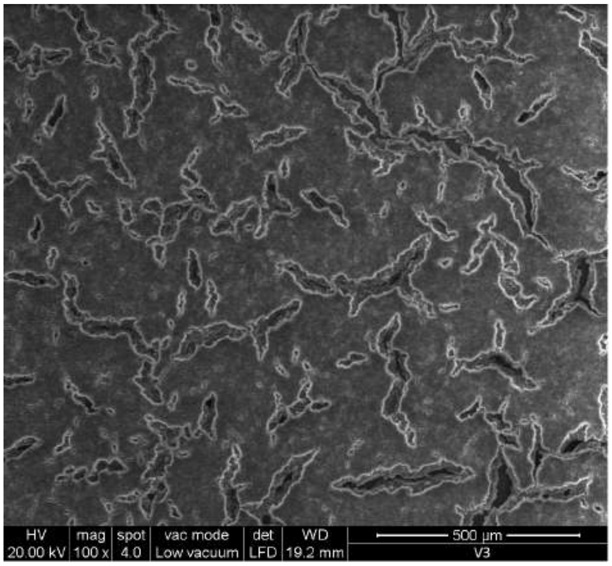

Figure 4.13: SEM image of MgO coating for dipping velocity of 40 cm/min.

As expected, an immersion speed of 10 cm/min means a lower thickness of the deposited layer with respect to the other velocities. Precisely, the thickness value of 76.7 nm related to the first specimen is not constant, probably because of the position of the sample during the drying and curing phases. Figure 4.9 shows the morphology of the coating, covered with many cracks. Nevertheless, several areas present a the firmly adhered layer. When increasing the dipping speed, the thickness of the layer consequently grows, but the risk that the coating has less adhesion to the underlying surface is enhanced as well. By the use of a dipping velocity of 20 cm/min, the thickness is increased to 156 nm. The SEM Figure 4.11 points out the existence of several evident cracks. Their presence is also probably due to the granular state of the magnesium oxide precursor.

Finally, the layer generated using a speed of 40 cm/min presents a thickness of 470 nm. The film thickness plays an important role in the resulting SEEY value. Value of the thickness ranging between 10 and 100 nm are the most common found in literature [44] [45] [46]. For this reason, no further investigation has been conducted with dip coating speeds higher than 20 cm/min. In addition, a bigger thickness could negatively affect the adhesion of the layer on the underlying substrate.

4.4 Deposition of $\mathbf{TiO_2}$ and $\mathbf{MgO+TiO_2}$

More tests were performed with coatings realized with TiO_2 and multilayered $MgO - TiO_2$, as proved by literature in Chapter 2. The same procedure as described in the last section was applied to these samples. In this case, the titania solution for the sol-gel method is composed of 4.5 ml of titanium isopropoxide ($Ti(OC_4H_9)_4$ liquid, purity $\geq$ 97%), 10 ml of n-propanol (C_3H_8O anhydrous, purity $\geq$ 99.5%) and 1.6 ml of acetil acetone (AcAc, $CH_3COCH_2COCH_3$, purity $\geq$ 99%). The resulting compound has been stirred at room temperature for one hour. Successively, a solution composed of 1.613 ml of n-propanol and 0.187 of water was added for any ml of the stock solution. The mixture was stirred again at room temperature for 2 hours. Then the coating layer has been deposited on the samples using th dip coating device.

Following the previous steps, the TiO_2 double layer and the multi-layered MgO-TiO_2 were created with a dipping speed of 10 cm/min as regards the first coat. After the deposition of the first layer, the specimens underwent a heat treatment, consisting in a heating ramp of 10^o/min until they reached the temperature of 500 ^{o} C. Successively, the temperature was kept still for 1 hour and then gradually decreased with another ramp of 10 ^{o}/min. This process allowed for the generation of MgO in one case and TiO_2 in the other case. Finally, the second titania film was deposited on both of the samples. The dipping speed applied for the second layer is 5 cm/min. Thus, the samples were submitted at the second heat treatment and the results are visible in the following pages.

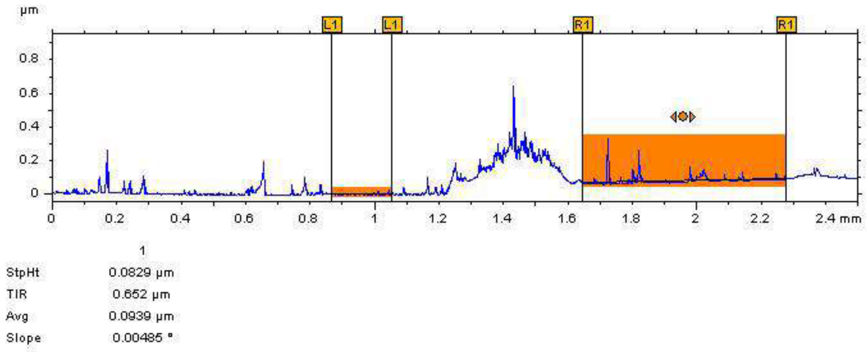

```
            1
StpHt       0.0829 µm
TIR         0.652 µm
Avg         0.0939 µm
Slope       0.00485 °
```

Figure 4.14: Profilometer result for first titania layer with dipping velocity of 10 cm/min. TiO_2 first layer thickness = 82.9 nm.

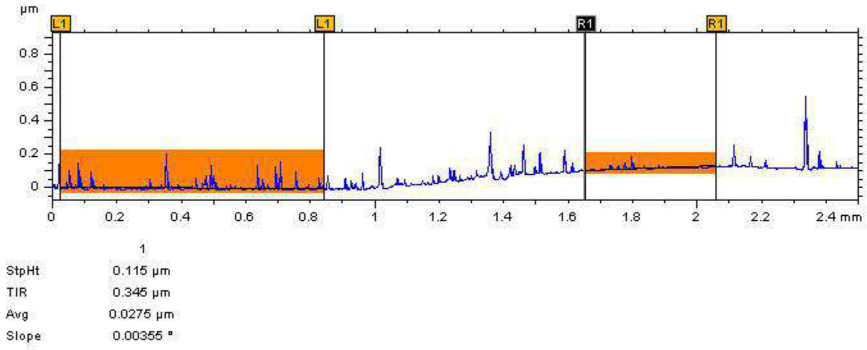

```
            1
StpHt       0.115 µm
TIR         0.345 µm
Avg         0.0275 µm
Slope       0.00355 °
```

Figure 4.15: Profilometer result for second titania layer with dipping velocity of 5 cm/min. TiO_2 second layer thickness = 115 nm.

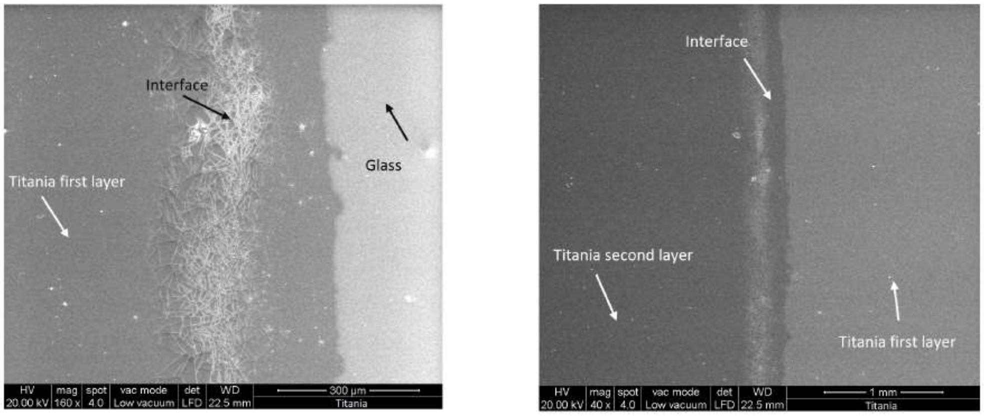

Figure 4.16: SEM images of the interface between glass and the first (left) and second (right) layer of TiO_2 coating.

The analysis with profilometer (4.14) underlines a first layer titania thickness of 82.9 nm. The study contucted by the SEM (Figure 4.16) shows a clear definition of the interface between the first layer of TiO_2 (left side of the image) and the glass (brighter area) substrate. The second layer presents a value of thickness equal to 115 nm (Figure 4.15). Even in this case the interface line between the first and second titania layer is precisely identifiable (right part of Figure 4.16). Unfortunately, the deposited films are characterized by several cracks, as it can be seen in detail in Figure 4.20. However, cracks are mostly limited to the interface area, while the rest of the deposition appears to be quite uniform and presents a rather constant thickness.

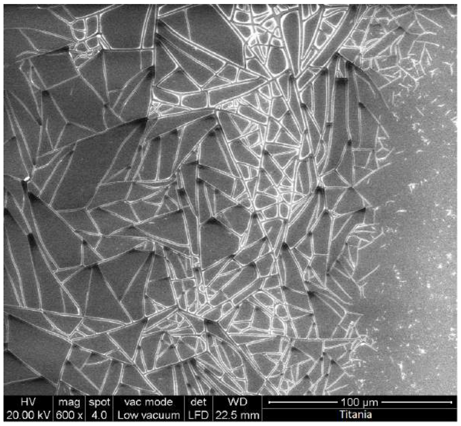

Figure 4.17: SEM image with focus on the interface area, characterized by several cracks, however restricted in this area.

As regards the multi-layered $MgO-TiO_2$ coating, the experiments performed the following results.

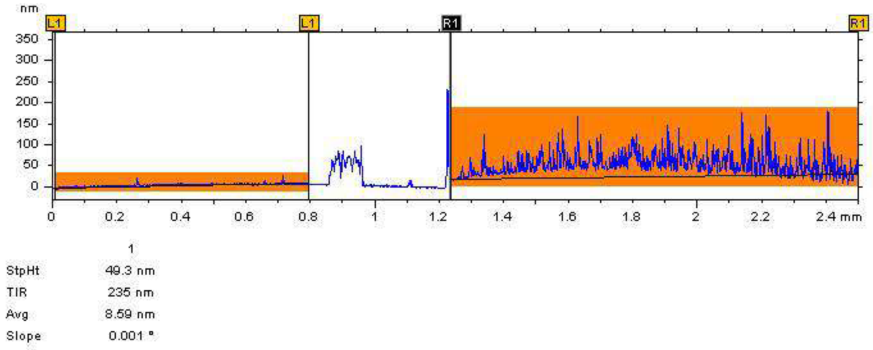

	1
StpHt	49.3 nm
TIR	235 nm
Avg	8.59 nm
Slope	0.001 °

Figure 4.18: Profilometer result for first MgO layer with dipping velocity of 10 cm/min. MgO layer thickness = 49.3 nm.

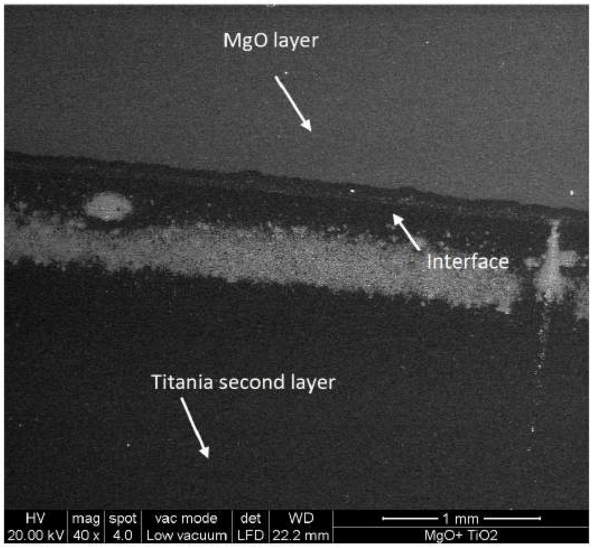

Figure 4.19: SEM image of the interface between MgO layer and the second TiO_2 layer.

Unfortunately, the analysis at profilometer only detected the MgO thickness, which presents a value of 49.3 nm (Figure 4.18). Nevertheless, from the SEM Figure 4.19 it can be seen quite clearly that TiO_2 layer was not only deposited, but shows a uniform adhesion as well, except for the interface area, where several cracks can be noticed (Figure 4.20). Probably, such cracks are due to an accumulation of the material in the interface zone while performing the phases of drying and heat treatment.

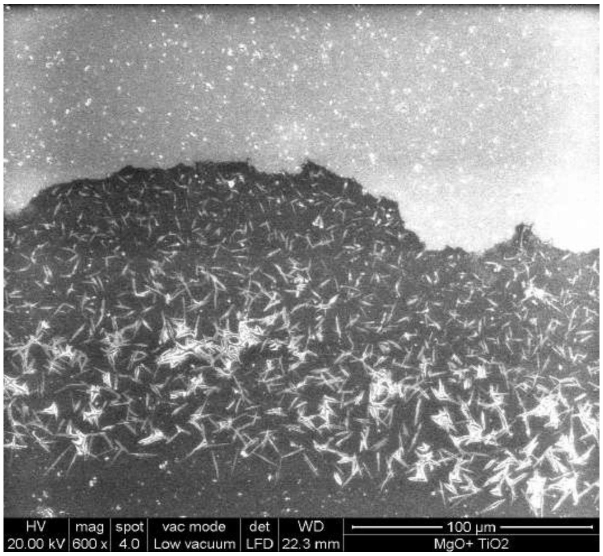

Figure 4.20: SEM image with focus on the interface between MgO and TiO_2 layers.

4.5 Deposition on Electrodes

This section is dedicated to the description of the deposition tests made on sample electrodes and the relative outcomes.

4.5.1 Sol-Gel Deposited Electrodes

An attempt was made to perform the sol-gel deposition of a MgO film on hollow Nichel electrodes. The process that has been followed is exactly the same as described in the previous experiments.

Taking into account the aim of this study and considering that these tests were the first for the present application, no attention was paid to the position of the electrodes during the drying phase. Moreover, it was supposed that some accumulation of the solution within the cathode would have helped secondary emission by enhancing the sputtering phenomenon. As the adoption of a coating thick enough seemed to reduce performance degradation, the prepared samples presented 5 layers of MgO coating.

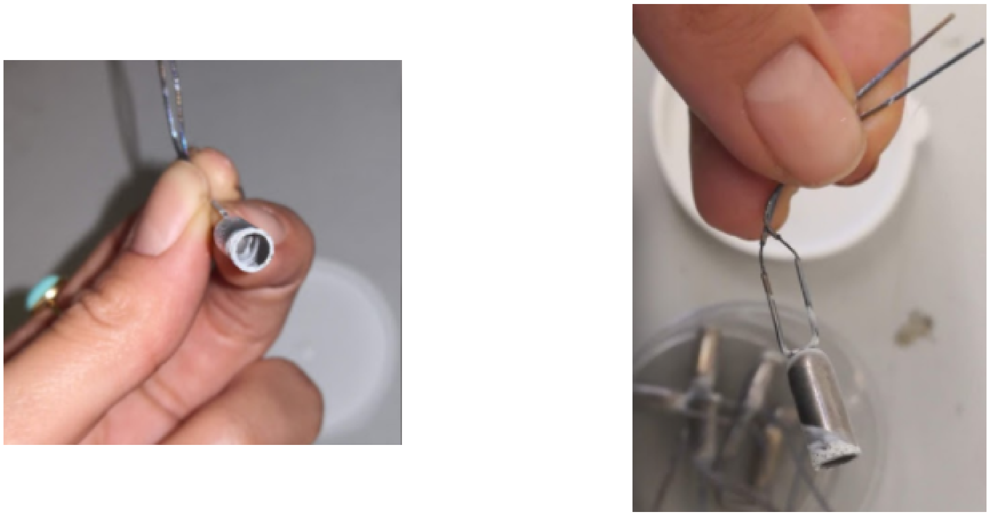

Figure 4.21: Sol-gel deposited electrodes.

Unfortunately, there was no possibility to realize complete vessels using sol-gel coated electrodes immersed in Argon. The firs encountered problem was precisely the just mentioned non-uniformity of the deposited film. Indeed, the formation of bubbles led to not-uniformities. Moreover, the dip-coating procedure is intrinsecally not uniform in such a geometry. The second issue is related to oxidation: during the curing and the heating phases, oxidation occurred. This could strongly compromise the glass-metal soldering.

4.5.2 Pellet Deposited Electrodes

Pellet samples were created by means of a *Atlas Manual Hydraulic Press 15T* by Specac (Figure 4.22).

Figure 4.22: Manual Hydraulic Press 15T used for the creation of pellets.

A large variety of pellets were created with different compositions, i.e. MgO, TiO_2, $MgO + TiO_2$ and Al_2O_3 respectively with a pressure of 3, 5 and 10 tons. However, due to the limited time and resources available, only the MgO pellet created with a pressure of 10 tons was tested (Figure 4.23). The reason of this choice lays in the fact that almost every pellet made by Al_2O_3 or containing TiO_2 underwent some sort of crumbling. This phenomenon may be caused by the different dimension of the granules between MgO powder and TiO_2 and Al_2O_3 precursors. Indeed, these two last powders present a much more thinner composition of the granules, thus explaining their inclination to crumbling.

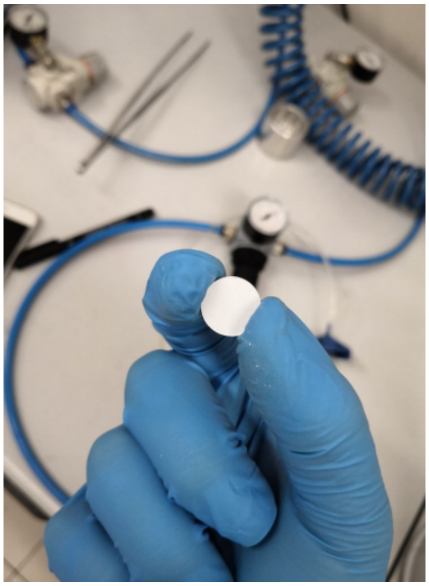

Figure 4.23: MgO pellet - pressure 10 tons.

The MgO pellet was fixed at the extremity of the hollow cathode by means of a MgO powder (Figure 4.24). Mixing 100 parts of such powder with 13 parts of water, the result, after 24 hours of rest at room temperature, is a highly dense blend that plays the role of a strong adhesive once solidified.

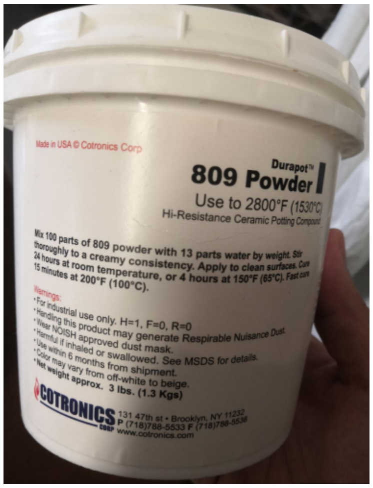

Figure 4.24: MgO powder used to fix the pellet to the electrode extremity.

Density Measures

Two phials were prepared with the pellet-deposited electrodes, filled with Argon at 2 mbar. In this section the phase plots and the plasma-density diagrams will be presented. Concerning the phase plots, two acquisitions per test were made in order to better observe the phase jumps: the first between 0 and 10 sec and the second one between 10 an 20 sec.

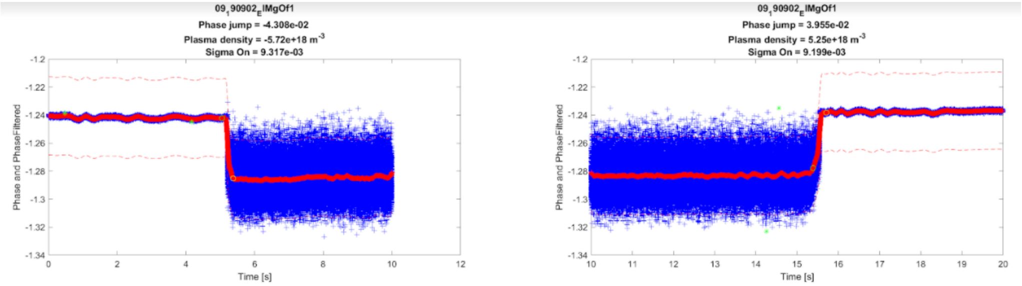

Figure 4.25: Phase plot for benchmark phial 1 for 20 sec density test. Qualitative phase jump analysis at the beginning and at the end of the test. X-axis reports time scale, Y-axis reports phase value.

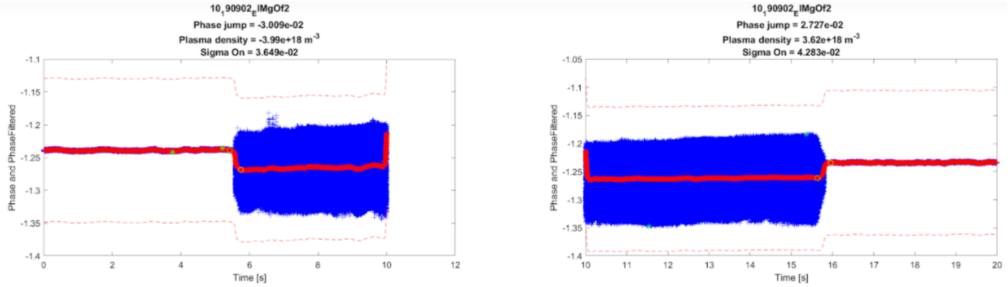

Figure 4.26: Phase plot for benchmark phial 2 for 20 sec density test. Qualitative phase jump analysis at the beginning and at the end of the test. X-axis reports time scale, Y-axis reports phase value.

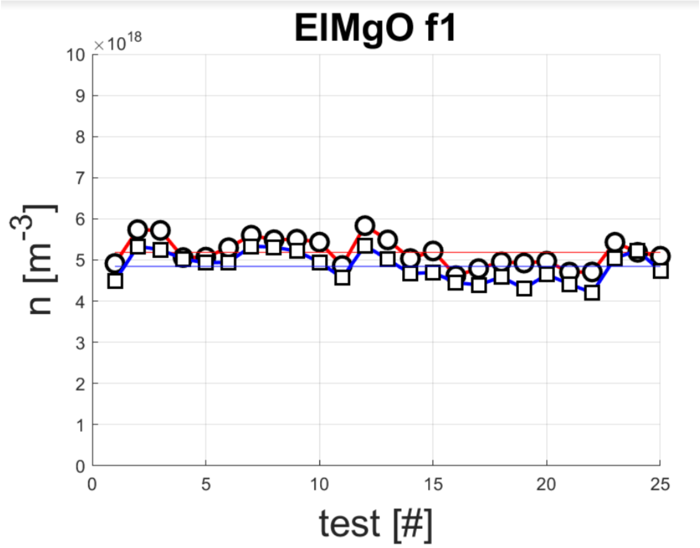

Figure 4.27: Benchmark density values for 20 sec ON-OFF tests on phial 1. X-axis indicates the test sequence, Y-axis shows density valuea. Measurement error on the density ≈ 10%.

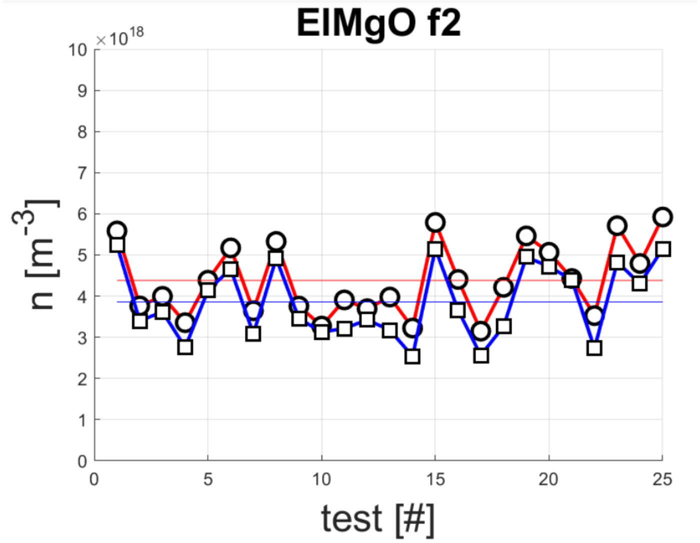

Figure 4.28: Benchmark density values for 20 sec ON-OFF tests on phial 2. X-axis indicates the test sequence, Y-axis shows density valuea. Measurement error on the density ≈ 10%.

In Figures 4.27 and 4.28, circles indicate the ON phase, while squares show the density value at the OFF phase. Red and blue straight lines display the mean density values respectively at the ON and OFF phase. As clearly visible from Figures 4.27 and 4.28, the trend is not as expected. Phial 1 behaves slightly better than phial 2, showing higher density values and a stabler trend. However, such results are not meliorative than the values obtained with un-coated electrodes having equal vessels and gas pressures. Indeed, while un-coated samples reached density values just below 10^{19}, with a mean value above $7 \cdot 10^{18}$, the best result of pellet-deposited phials reaches $6 \cdot 10^{18}$, with a mean value just above $5 \cdot 10^{18}$.

The reasons behind this outcome can be several. One of the problems can surely be the very low control on the solidification process of the adhesive powder. Moreover, it may happen that the powder solidifies over the pellet surface thus dampening the secondary emission due to sputtering, that the pellet has instead the aim to enhance. In addition, the pellet may encounter difficulties in the sputtering of MgO particles throughout the vessel because of the too high pressure applied to the pellet, thus making it too compact and solid and limiting the power penetration of electrons and ions. Finally, the thickness of the MgO substrate generated at the end of the electrode by the pellet and the adhesive powder could strongly contain the particles motion through the cathode.

CHAPTER 5

Conclusions

In this study several topics have been debated:

- The first effort was mad in the direction of searching for materials and compounds with the aim of enhancing the plasma density. The selection had to take into account the right compromise between secondary emission properties and the material cost and availability.
- The following step has been to compare electrodes of different dimensions, i.e. T7 and T10, with the latter (having a bigger diameter) performing the best results in terms of electron density.
- At this point, electrode deposition of the compounds found in literature is examined in order to increase the intrinsic emission properties of such materials. The procedures chosen to realize this scope are the pellet coated electrodes and the sol-gel method, explained in detail with several examples of coating on of glass substratum. In addition, SEM and profilometer analysis of morphology and thickness of the coated layers brought a great support to the research.
- Finally, practiacl tests of the hypothesized ideas were realized. Precisely, the attempts concerning the sol-gel coated electrodes were inconclusive due to oxidation problems occurred during the curing and

heating phases, which strongly compromised the glass-metal soldering. Plasma density measurement for the pellet-coated cathodes were reported and compared to the un-coated vessels. However, outputs were not satisfying as the density values resulting from pellet-coated cathodes were pejorative than un-coated ones.

Even though tests conducted on samples of coated electrodes have not brought to the desired results, they establish a strong starting point in order to lay the foundation to further researches and developments. The sol-gel method have proven to be a really strong instrument as it produces interesting results with low effort and cost. Moreover, it is quite a reliable and repeatable process. The pellet-coated electrode has been a risky experiment with a very low literature background. However, this study has proven that the basis for better improvements and more reliable processes are concrete.

Several suitable materials for the GPAs applications have been found: MgO, TiO_2, Al_2O_3. These materials have provided excellent results when used to coat the glass substratum of cylindrical tubes. Further studies on the morphology and thickness of deposited coating are advisable, as well as exploring other deposition methods. A promising possible idea could be achieved by investigating the use of 3D-printed ceramic electrodes. 3D printing would be an interesting resource in terms of lowering costs and manufacture complexity.

One of the most interesting compound is barium titanate ($BaTiO_3$). It is a ferroelectric ceramic material with piezoelectric properties and presents a perovskite crystal structure.

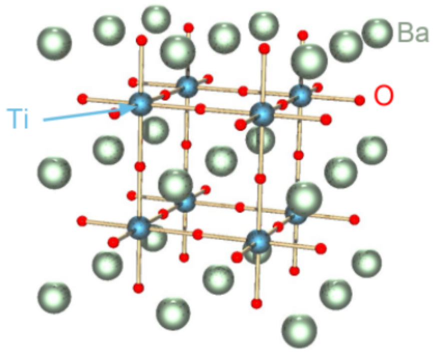

Figure 5.1: $BaTiO_3$ perovskite crystal structure.

Thin films of $BaTiO_3$ can be used in several applications, such as the conversion of mechanical energy into electrical energy [47]. When doped with rare earths, they become semiconductors used for PCBs (printed circuit boards). The properties of donor-doped $BaTiO_3$ electrodes are described in [48]. Therefore, $BaTiO_3$ electrodes could be conductive and provide secondary emission. Thin $BaTiO_3$ films can be generated by a wide variety of processes, such as atomic layer deposition [49], vapor deposition [50], hydrothermal electromechanical method [51], sol-gel method [52].

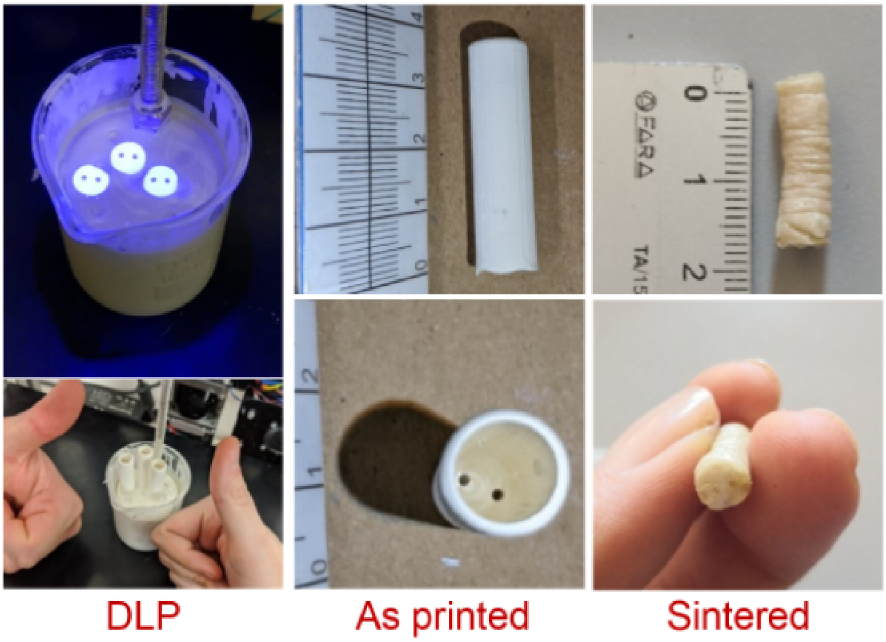

Figure 5.2: $BaTiO_3$ electrode prototypes.

The future goal would be to achieve double-layer electrodes with outer conductive metal shell and inner ceramic core. This highlights a first possible issue: specific combinations of ceramic and metallic compositions that have matching thermal expansion coefficients will be needed. Moreover, thermal treatments could induce cracks and deformations. Double-layer electrodes could be created by means of dual material extrusion: electrode and ceramic coating could be deposited simultaneously with high accuracy. The problem related to the manufacturing process is that the multi-material extrusion system still needs to be implemented. In addition, the choice of the two materials is critical as they should meet both process and application requirements. Further optimization is needed, but such application could represent the right step towards the improvement of plasma antennas.

Bibliography

[1] F. F. Chen, *Introduction to plasma physics and controlled fusion.* Springer, 1984, vol. 1.

[2] J. A. Bittencourt, *Fundamentals of plasma physics.* Springer Science & Business Media, 2013.

[3] I. L. Alberts, D. S. Barratt, and A. K. Ray, "Hollow cathode effect in cold cathode fluorescent lamps: a review," *Journal of display technology*, vol. 6, no. 2, pp. 52–59, 2010.

[4] A. Fridman, *Plasma chemistry.* Cambridge university press, 2008.

[5] D.-G. Fang, *Antenna theory and microstrip antennas.* CRC Press, 2017.

[6] C. A. Balanis, *Antenna theory: analysis and design.* John wiley & sons, 2016.

[7] A. A. Kishk, "Fundamentals of antennas," *Ch. 1 on Antennas for Base Stat. in Wireless Comm.*, pp. 1–30, 2009.

[8] C. A. Balanis, "Antenna theory," 2005.

[9] D. Melazzi, V. Lancellotti, and A.-D. Capobianco, "Analytical and numerical study of a gaseous plasma dipole in the uhf frequency band," *IEEE Transactions on Antennas and Propagation*, vol. 65, no. 12, pp. 7091–7101, 2017.

[10] D. Melazzi, P. De Carlo, F. Trezzolani, M. Manente, A.-D. Capobianco, and S. Boscolo, “Beam-forming capabilities of a plasma circular reflector antenna,” *IET Microwaves, Antennas & Propagation*, vol. 12, no. 15, pp. 2301–2306, 2018.

[11] T. Anderson, *Plasma antennas.* Artech House, 2011.

[12] G. Mansutti, P. De Carlo, A.-D. Capobianco, D. Melazzi, F. Trezzolani, and A. Tuozzi, “L-band plasma turnstile antenna for gps applications,” in *2019 13th European Conference on Antennas and Propagation (EuCAP).* IEEE, 2019, pp. 1–5.

[13] D. M. Goebel and I. Katz, *Fundamentals of electric propulsion: ion and Hall thrusters.* John Wiley & Sons, 2008, vol. 1.

[14] I. L. Alberts, D. S. Barratt, and A. K. Ray, “Cold cathode sputtering in glow discharges,” *Journal of Display Technology*, vol. 8, no. 8, pp. 450–456, 2012.

[15] W. B. Nottingham, R. Good, E. W. Müller, R. Kollath, G. Weissler, W. Allis, L. Loeb, A. von Engel, and P. Little, “Electron-emission gas discharges i/elektronen-emission gasentladungen i,” *Handbuch der Physik*, vol. 21, 1956.

[16] P. Sigmund, “Theory of sputtering. i. sputtering yield of amorphous and polycrystalline targets,” *Physical review*, vol. 184, no. 2, p. 383, 1969.

[17] M. Tartz, T. Heyn, C. Bundesmann, and H. Neumann, “Measuring sputter yields of ceramic materials,” in *31st Int. Electr. Propuls. Conf*, no. 240, 2009, pp. 1–14.

[18] A. Yalin, B. Rubin, S. Domingue, Z. Glueckert, and J. Williams, “Differential sputter yields of boron nitride, quartz, and kapton due to low energy xe+ bombardment,” in *43rd AIAA/ASME/SAE/ASEE Joint Propulsion Conference & Exhibit*, 2007, p. 5314.

[19] T. Tondu, V. Viel-Inguimbert, J. Roussel, and S. D’Escrivan, “Hall effect thrusters ceramics sputtering yield determination by monte carlo simulation,” in *44th AIAA/ASME/SAE/ASEE Joint Propulsion Conference & Exhibit*, 2008, p. 5090.

[20] B. Rubin, J. L. Topper, and A. P. Yalin, “Total and differential sputter yields of boron nitride measured by quartz crystal microbalance and weight loss,” in *30th International Electric Propulsion Conference*, vol. 74, 2007.

[21] A. Semenov and I. Shkarban, “Ion beam sputtering of the surfaces of ion and plasma sources,” *Rocket and Space Engineering: Rocket Engines and Power Plants*, vol. 3, pp. 42–53, 1991.

[22] Y. Garnier, V. Viel, J.-F. Roussel, and J. Bernard, “Low-energy xenon ion sputtering of ceramics investigated for stationary plasma thrusters,” *Journal of Vacuum Science & Technology A: Vacuum, Surfaces, and Films*, vol. 17, no. 6, pp. 3246–3254, 1999.

[23] V. V. Abashkin, O. A. Gorshkov, A. S. Lovtsov, and A. A. Shagaida, “Analysis of ceramic erosion characteristic in hall-effect thruster with higher specific impulse,” in *International Electric Propulsion Conference*, 2007, pp. 2007–133.

[24] J. Topper, B. Rubin, C. Farnell, and A. Yalin, “Preliminary results of low energy sputter yields of boron nitride due to xenon ion bombardment,” in *44th AIAA/ASME/SAE/ASEE Joint Propulsion Conference & Exhibit*, 2008, p. 5092.

[25] K. Gschneidner, “Solid state phys. advances in research and applications (eds) f seitz and d turnball,” *New York: Academic Press*, vol. 16, p. 412, 1964.

[26] J. Devooght, A. Dubus, and J.-C. Dehaes, “Improved age-diffusion model for low-energy electron transport in solids. i. theory,” *Physical Review B*, vol. 36, no. 10, p. 5093, 1987.

[27] R. O. Jenkins and W. G. Trodden, *Electron and ion emission from solids.* Dover Publications, 1965.

[28] C. E. Huerta and R. E. Wirz, “Surface geometry effects on secondary electron emission via monte carlo modeling,” in *52nd AIAA/SAE/ASEE Joint Propulsion Conference*, 2016, p. 4840.

[29] A. Shih, J. Yater, P. Pehrsson, J. Butler, C. Hor, and R. Abrams, "Secondary electron emission from diamond surfaces," *Journal of applied physics*, vol. 82, no. 4, pp. 1860–1867, 1997.

[30] Y. Yong, J. Thong, and J. Phang, "Determination of secondary electron yield from insulators due to a low-kv electron beam," *Journal of applied physics*, vol. 84, no. 8, pp. 4543–4548, 1998.

[31] N. R. Whetten and A. Laponsky, "Secondary electron emission of single crystals of mgo," *Journal of Applied Physics*, vol. 28, no. 4, pp. 515–516, 1957.

[32] ——, "Secondary electron emission from mgo thin films," *Journal of Applied Physics*, vol. 30, no. 3, pp. 432–435, 1959.

[33] Y. Kishimoto, T. Hayashi, M. Hashimoto, and T. Ohshima, "Secondary electron emission from polymers and its application to the flexible channel electron multiplier," *Journal of Applied Polymer Science*, vol. 21, no. 10, pp. 2721–2733, 1977.

[34] X. Zhang, D. den Engelsen, K. Raper, and W. Lei, "Lumen efficiency of cold cathode fluorescent lamp (ccfl) improvement with mgo coated cathode," in *2006 IEEE International Vacuum Electronics Conference held Jointly with 2006 IEEE International Vacuum Electron Sources.* IEEE, 2006, pp. 131–132.

[35] J.-W. Lee, S.-H. Jung, M.-K. Lee, S.-J. Jung, H.-S. Song, E.-H. Choi, and G. Cho, "P-84: Cold cathode fluorescent lamps with mgo-coated electrode," in *SID Symposium Digest of Technical Papers*, vol. 40, no. 1. Wiley Online Library, 2009, pp. 1434–1437.

[36] D. den Engelsen and X. Zhang, "Improving the cold cathode fluorescent lamp," in *2010 8th International Vacuum Electron Sources Conference and Nanocarbon.* IEEE, 2010, pp. 107–108.

[37] S. J. Jokela, I. V. Veryovkin, A. V. Zinovev, J. W. Elam, A. U. Mane, Q. Peng, Z. Insepov *et al.*, "Secondary electron yield of emissive materials for large-area micro-channel plate detectors: surface composition and film thickness dependencies," *Physics Procedia*, vol. 37, pp. 740–747, 2012.

[38] G. Mearini, I. Krainsky, J. Dayton Jr, Y. Wang, C. A. Zorman, J. C. Angus, R. Hoffman, and D. Anderson, “Stable secondary electron emission from chemical vapor deposited diamond films coated with alkali-halides,” *Applied physics letters*, vol. 66, no. 2, pp. 242–244, 1995.

[39] O. Tudisco, A. Lucca Fabris, C. Falcetta, L. Accatino, R. De Angelis, M. Manente, F. Ferri, M. Florean, C. Neri, C. Mazzotta *et al.*, “A microwave interferometer for small and tenuous plasma density measurements,” *Review of Scientific Instruments*, vol. 84, no. 3, p. 033505, 2013.

[40] S. Sakka and H. Kozuka, *Handbook of sol-gel science and technology. 1. Sol-gel processing.* Springer Science & Business Media, 2005, vol. 1.

[41] A. C. Pierre, *Introduction to sol-gel processing.* Springer Nature, 2020.

[42] K. Tadanaga, N. Katata, and T. Minami, “Formation process of super-water-repellent al2o3 coating films with high transparency by the sol–gel method,” *Journal of the American Ceramic Society*, vol. 80, no. 12, pp. 3213–3216, 1997.

[43] E. Storti, M. Roso, M. Modesti, C. G. Aneziris, and P. Colombo, “Preparation and morphology of magnesium borate fibers via electrospinning,” *Journal of the European Ceramic Society*, vol. 36, no. 10, pp. 2593–2599, 2016.

[44] R. Kim, Y. Kim, and J.-W. Park, “Improvement of secondary electron emission property of mgo protective layer for an alternating current plasma display panel by addition of tio2,” *Thin Solid Films*, vol. 376, no. 1-2, pp. 183–187, 2000.

[45] S. J. Rho, S. M. Jeong, H. K. Baik, and K. M. Song, “The structural, optical and secondary electron emission properties of mgo and mg–o–cs thin films prepared by ion beam assisted deposition,” *Thin Solid Films*, vol. 355, pp. 55–59, 1999.

[46] J. Lee, T. Jeong, S. Yu, S. Jin, J. Heo, W. Yi, D. Jeon, and J. Kim, “Thickness effect on secondary electron emission of mgo layers,” *Applied surface science*, vol. 174, no. 1, pp. 62–69, 2001.

[47] K.-I. Park, S. Xu, Y. Liu, G.-T. Hwang, S.-J. L. Kang, Z. L. Wang, and K. J. Lee, "Piezoelectric batio3 thin film nanogenerator on plastic substrates," *Nano letters*, vol. 10, no. 12, pp. 4939–4943, 2010.

[48] T. Kutty and L. G. Devi, "Photoelectrochemical properties of donor doped batio3 electrodes," *Materials research bulletin*, vol. 20, no. 7, pp. 793–801, 1985.

[49] M. Vehkamäki, T. Hatanpää, T. Hänninen, M. Ritala, and M. Leskelä, "Growth of srtio3 and batio3 thin films by atomic layer deposition," *Electrochemical and Solid State Letters*, vol. 2, no. 10, p. 504, 1999.

[50] B. Kwak, K. Zhang, E. Boyd, A. Erbil, and B. Wilkens, "Metalorganic chemical vapor deposition of batio3 thin films," *Journal of applied physics*, vol. 69, no. 2, pp. 767–772, 1991.

[51] M. Yoshimura, S.-E. Yoo, M. Hayashi, and N. Ishizawa, "Preparation of batio3 thin film by hydrothermal electrochemical method," *Jpn. J. Appl. Phys*, vol. 28, no. 11, pp. L2007–L2009, 1989.

[52] T. Hayashi, N. Oji, and H. Maiwa, "Film thickness dependence of dielectric properties of batio3 thin films prepared by sol-gel method," *Japanese journal of applied physics*, vol. 33, no. 9S, p. 5277, 1994.